Synthesis and Characterization of New Solid-State Li-Superionic Conductors

by

Laidong Zhou

A thesis

presented to the University of Waterloo

in fulfillment of the

thesis requirement for the degree of

Master of Science

in

Chemistry-Nanotechnology

Waterloo, Ontario, Canada, 2017

AUTHOR'S DECLARATION

I hereby declare that I am the sole author of this thesis. This is a true copy of the thesis, including any required final revisions, as accepted by my examiners.

I understand that my thesis may be made electronically available to the public.

Abstract

Compared with lithium ion batteries which use liquid electrolyte, all solid-state lithium batteries (ASSLBs) show great potential in improving the safety and achieving both high power and energy densities. This has driven researchers to make a lot of efforts to develop the ASSLB technologies. However, much work still has to be done on the selection and modification of solid electrolyte candidates. In addition, traditional solid-state reactions that are widely used to synthesize solid electrolytes generally cost high and are hard to scale-up. Thus, the development of cost-effective and simple synthesis method, in addition to the discovery of new solid electrolytes, is important to move this field forward.

Solid state electrolytes are the essential component for high energy density ASSLBs. Argyrodite materials Li_6PS_5X (X=Cl, Br) are one of the best candidates due to their high ionic conductivity and the ability to form a stable interphase with a Li metal anode as well as some lithium transition metal oxide cathode materials. Nevertheless, new synthesis methods beyond traditional all solid state approaches are required to reduce the cost and promote scale-up. Herein, I report a direct solution-based synthesis of argyrodites Li_6PS_5X (X = Cl, Br, I), as discussed in Chapter 3, with 100% degree of crystallinity. The solid electrolytes show high ionic conductivities up to 2×10^{-3} S/cm for X = Cl, Br and negligible electronic conductivities. This solution synthesis method is not only scalable, but also provides new insight into simple synthesis of other halide-thiophosphate based solid electrolytes. The argyrodite Li_6PS_5I shows a poorer ionic conductivity but can be increased by antimony-doping. The doping would also

improve the stability of the solid electrolytes against air and moisture. Antimony-doping will change the unit cell size and halogen disorder. The effects of unit cell size and halogen disorder are investigated to study the origin of the high ionic conductivity in the argyrodite phases.

Chapter 4 discusses the synthesis of $Li_3Y(PS_4)_2$ and $Li_6Y_3(PS_4)_5$ which can be potentially used as solid electrolytes. Phase pure $Li_6Y_3(PS_4)_5$ was successfully synthesized, however a relatively low conductivity 3.6×10^{-6} S/cm was obtained. The effect of aliovalent doping, which can introduce Li-ion interstitials and vacancies into the lattice, was investigated with Ca^{2+} or Zr^{4+} doping into the Y^{3+} site. Slightly increased conductivity was obtained for Ca^{2+} doping, but a decreased conductivity was shown for Zr^{4+} doping. The low conductivities in all cases is possibly due to the low crystallinity of the products. Further modification of synthesis conditions could further improve the ionic conductivity.

Acknowledgements

I would like to express my sincere gratitude to my supervisor Dr. Linda F. Nazar for her tremendous guidance and support in the past two years of my graduate study. It was a wonderful time and I am looking forward to next several years PhD study.

I would also extend my appreciations to Dr. Guang He for his help and guidance in my early career after I joined this group. It was a great experience to work with him, as I learnt a lot form his brilliant ideas and ways of solving problems. Furthermore, I would also like to thank Dr. Xiaoqi Sun, Dr. Quanquan Pang, Dr. Xiao Liang for their fruitful discussion and generous help in science and bringing me joy outside the lab.

I would like to thank my master committee: Dr. Pavle Radovanovic, Dr. Vivek Maheshwari for their guidance on my research. I would like to thank the solid state team: Dr. Fabien Lalère, Dr. Zhizhen Zhang, Kavish Kaup, and Erika Paola Ramos Guzman for the great discussion on solid electrolyte project and Abhinandan Shyamsunder and Chun Yuen Kwok for their help in experiments. Also my thanks to the rest of the group for their help and building a nice working atmosphere in the lab.

Finally, I would like thank my parents who brought me up for their love, selfless support and encouragement.

Table of Contents

List of Figures

List of Tables

List of Abbreviations

AC	Alternating current
ACN	Acetonitrile
ASSLBs	All solid-state lithium batteries
CI-NEB	Climbing images nudged elastic band
DC	Direct current
DEC	Diethyl carbonate
DFT	Density functional theory
DMC	Dimethyl carbonate
DME	1,2-dimethoxyethane
EC	Ethylene carbonate
EIS	Electrochemical impedance spectroscopy
ICSD	Inorganic crystal structure database
LGPS	$Li_{10}GeP_2S_{12}$
LiPON	$Li_{3.3}PO_{3.9}O_{0.17}$
LiTFSI	Bis(trifluoromethane) sulfonimide
MD	Molecular dynamics
NMC	$LiNi_{1/3}Mn_{1/3}Co_{1/3}O_2$
PDF	Probability density function
SEI	Solid electrolyte interphase
SEM-EDX	Scanning electron microscopy- Energy dispersive X-ray spectroscopy
SS	Stainless steel
THF	tetrahydrofuran
XPS	X-ray photoelectron spectroscopy
XRD	X-ray diffraction

Chapter 1 Introduction

1.1 Overview of Rechargeable Lithium Batteries

Modern civilization has been mainly depending on energy from fossil fuels over last several decades. At the same time, the rapid increase of the earth's population has resulted in a dramatically increased demand for fossil fuel energy. The finite supply and uneven distribution of fossil fuel globally will impede the economic development.[1] On the other side, the massive production of CO_2 and other pollutants from fossil fuels have caused severe environment problems, among which are global warming and air pollution. They have already become two of the most severe challenges facing human society today.[2] Limited fossil fuel resources and the environmental impact of their use require a change to renewable energy sources in the near future.

Alternative energy generation technologies, such as wind and solar energy, are being adopted and popularized worldwide. However, these renewable energy resources are only intermittently available and dependent on the time, weather, seasons, and locations, while the demand and consumption of electric energy are relatively constant with respect to daily use. Energy storage systems are therefore required to store these intermittent energy sources which then can be further used in powering electronics and electrical devices such as cellphones and electric vehicles. Rechargeable batteries have been considered to be one of the best candidates for energy storage. Among the existing rechargeable battery technologies, Lithium ion batteries currently dominate the energy storage market due to their low weights and high specific energy densities.[2,3,4]

1

1.1.1 Terminologies

Rechargeable (secondary) batteries can be reversibly charged and discharged for certain duration (life-time), opposed to primary batteries (one-time use). A battery is essentially many electrochemical cells connected in series or parallel to provide voltage or current.[5] Most researchers in the field of science are focused on improving the electrochemical performance of an individual electrochemical cell. Each cell contains a positive (cathode) electrode and negative (anode) electrode, separated by an electrolyte, with dissociated salt that allows ion transfer between electrodes.[6] In principle, the operation of a cell is based on the chemical potential difference of two active materials in electrodes, which induce the reduction and oxidation half reaction in cathode and anode during discharging. The electrodes should be both electrically and ionic conductive, as electron transfer and ion transportation occur on the surface and within the electrodes at the same time. The electrolyte is an ionic conductor and electric insulator, which can be either solid or liquid, rendering two types of batteries: traditional liquid containing batteries and all solid-state batteries. An electrolyte-permeable but insulating porous separator is needed for liquid electrolyte cells to avoid physical contact of the two electrodes, which will cause short circuit.

To evaluate the performance of a cell, there are some basic characteristics, including potential of electrodes and cell voltage, specific capacity, energy density, rate capacity, columbic efficiency and cycling life. These concepts are essential for understanding the work in this thesis:

2

Potential of electrode and cell voltage

The standard potential (E^o) of an electrode is determined by **Equation 1.1**

$$E^o = -\Delta G/nF \qquad\qquad \textbf{Equation 1.1}$$

Where the ΔG is the free energy change of the half reaction, n is the number of electrons involved in the half reaction and F is the Faraday's constant. The standard cell voltage V^o is the difference of the E^o of the two reactions ($V^o_{Cell} = E^o_{Cathode} - E^o_{Anode}$). The potential difference is desired to be large as the output powder is the product of cell voltage and current. This potential difference has to be within the stability potential window of the electrolyte that is in use, to prevent the electrolyte decomposition (reduction and oxidation). The real electrode potential is also depending on the other parameters, including ion concentration and temperature, as outlined in Nernst equation. The measured cell voltage during charging (discharging) is higher (lower) due to the over-potential, resulting from some limiting kinetic factors, such as ion migration, electron conduction.

Specific capacity

The specific capacity (mAh/g) or volumetric capacity (mAh/cm^3) of an electrode is defined as the number of charge (electrons or ions) that can be transferred per mass or volume of electrode material for one full charge/discharge. The obtained specific capacity of an electrode material is usually lower than the theoretical capacity due to the incomplete reaction. The discharge/charge voltage profile is a plot of voltage as a function of specific capacity

3

during the galvanostatic cycling of a cell, when a constant current is applied. The profiles revel information about the redox reactions and at what voltage they are occurring. Minimum voltage difference between discharge and charge (that is lowest polarization) is desired for maximizing energy efficiency (the ratio of dischargeable energy over charged energy).

Energy density

The total energy output from a cell is given by the product of capacity (mAh) and cell voltage (V). The energy density is defined by the energy output per mas (Wh/Kg) or volume (Wh/L) of materials. The calculation of energy density is usually based on the mass or the volume of the whole cell configuration, but it can also base on the mass/volume of a specific electrode or two electrodes, depending on specific situation.

Rate capacity

The current at which a cell is operated is usually a fraction of "C" rate as per mass of the working electrode. "1 C" rate means the theoretical specific capacity of this material is fully charged/discharged in one hour. Generally, discharging a cell at higher rate will give higher power, but lead to higher polarization, lower the energy efficiency and specific capacity.

Coulombic efficiency

The Coulombic Efficiency, expressed in %, is the ratio of the output (discharging) capacity to the input (charging) capacity of the same cycle. It provides an interesting analysis capacity retention over the number of cycles for prolonged galvanostatic cycling of a cell.

Cycling life

Cycling life of a cell means the number of cycles that it can survive with specified capacity retention. It is extremely important for the commercialized cells, as it is pertinent to its service life. For laboratory research, cycling life of a cell is usually examined by cycling (charging/discharging) a cell in a galvanostatic mode continuously until the capacity fades substantially. However, the practical operation conditions are more complicated, e.g. rate changes and rest time.

Among all the rechargeable battery systems, lithium ion batteries have dominated the market for decades, owing to their high cell voltage, low self-discharge rate and stable cycling performance.[2,3,4]

1.1.2 Lithium Ion Batteries

Lithium ion batteries are usually consisted of two electrodes, Positive electrode and negative electrode (cathode and anode), which are separated by the electrolyte. Conventionally, the cells contain a graphite anode and a lithium metal oxide cathode and rely on the lithium

5

ion intercalation/deintercalation mechanism.[6] For the lithium ion battery with graphite anode and $LiCoO_2$ cathode (as shown in **Figure 1.1**[6]), during charging, the positive Li^+ ions move from the cathode and enter the anode. Electrons pass through the external circuit thus generating power. The cathode compensates charge for the removal of the Li^+ ion by oxidizing the transition metal present in the lattice ($Co^{3+} \rightarrow Co^{4+}$). After Li^+ ions reach the graphite anode, they intercalate into graphite and recombine with electrons. When the cell is discharging, the reverse reactions occur. A representation of this process is shown in **Equation 1.2-1.5** summarize the reactions of a $LiCoO_2$/graphite cell:

Positive electrode (charge): $LiCoO_2 \rightarrow Li_{1-x}CoO_2 + x\ Li^+ + x\ e^-$ 　　　　　　　　1.2

Negative electrode (charge): $C_6 + x\ Li^+ + x\ e^- \rightarrow Li_xC_6$ 　　　　　　　　　　　　1.3

Positive electrode (discharge): $Li_{1-x}CoO_2 + x\ Li^+ + x\ e^- \rightarrow LiCoO_2$ 　　　　　　1.4

Negative electrode (discharge): $Li_xC_6 \rightarrow C_6 + x\ Li^+ + x\ e^-$ 　　　　　　　　　　　1.5
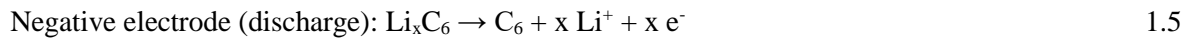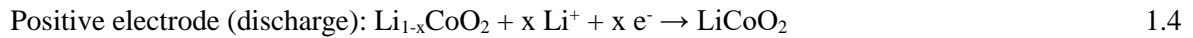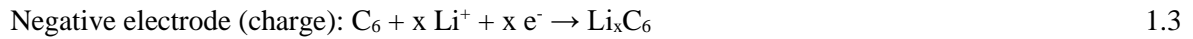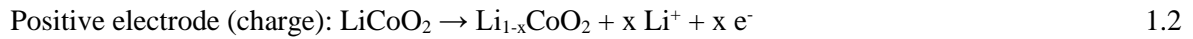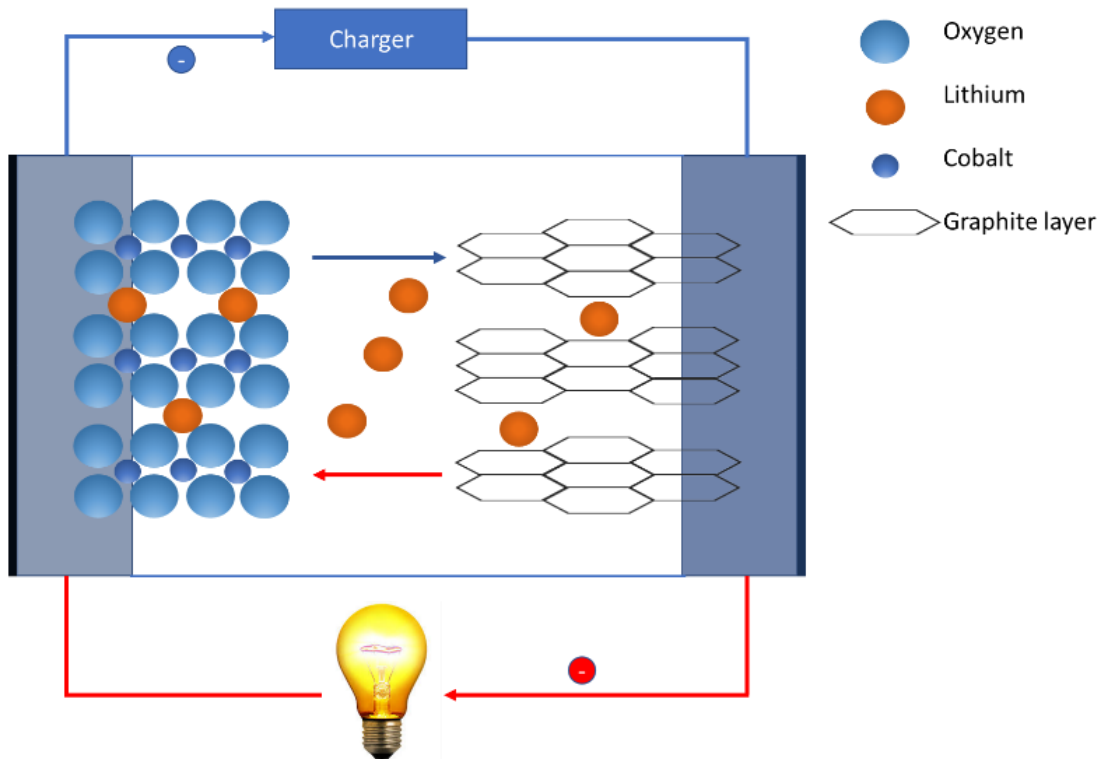
Figure 1.1: Schematic illustration of a typical lithium-ion battery that consists of layer structured LiCoO$_2$ and graphite as the cathode and anode, respectively. The electrolyte layer consisting of lithium salt(s) in the solvent(s) is in between the electrodes.

As mentioned earlier, traditional lithium ion batteries consist of three parts: cathode, anode and organic liquid electrolyte. The liquid electrolyte is composed of a lithium salt, typically $LiPF_6$ or bis(trifluoromethane) sulfonimide lithium salt (LiTFSI), dissolved in a mixture of linear and cyclic alkyl carbonates with an ionic conductivity of $\sim 10^{-2}$ S cm^{-1} at room temperature.[1] However, the intrinsic properties of organic liquid electrolytes lead to serious safety issues regarding their flammability and leakage risks, and thus require expensive sealing agents.[7] Another major problem is the formation of Li dendrite during long time cycling which may result in short-circuits and possibly explosions.[8] Besides, the low achievable specific energy density of lithium ion battery (100-220 Wh/Kg, 300-600 Wh/L) and high cost limit their applications, such as electric vehicle and large scale energy storage systems.[9, 10] Electrochemical systems that offers a higher capacity and energy density as well as a long cycling life at lower costs are desired, this leads to the development of the next generation batteries, typical example is lithium sulfur batteries.

1.2 Lithium-Sulfur Battery Overview

Lithium sulfur batteries are considered as one of the most promising candidates for the next generation energy storage systems, due to their high theoretical energy density, natural abundance of sulfur and low environmental concerns.[6,11,12,13] A conventional lithium sulfur battery contains a lithium metal anode and an elemental sulfur cathode with ether-based electrolyte, as shown in **Figure 1.2**.[14] . The overall redox couple of a Li-S cell is described by the **Equation 1.6**:

$$2 \text{ Li}^+ + 2\text{e}^- + \text{xS} \xtofrom[charge/discharge]{} Li_2S_x \quad 1 < x < 8 \qquad \textbf{Equation 1.6}$$
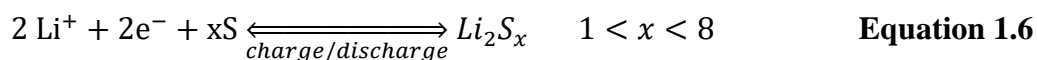
The coupling of high capacity lithium (3840 mAh/g) and sulfur (1675 mAh/g) offers an average cell voltage of 2.2 V and a theoretical specific energy 2570 Wh/Kg based on the two electrodes. The electrochemical reactions of lithium sulfur batteries are based on the reversible conversion reactions between sulfur and lithium sulfide, which are completely different from the traditional lithium ion batteries' lithium ion intercalation/deintercalation mechanism. The reversible conversion reaction between sulfur and lithium sulfide are always accompanied by a series of intermediate lithium polysulfides (Li_2S_n $2 \leq n \leq 8$), which are soluble in the ether-based electrolytes. During discharging and charging, the dissolved lithium polysulfide intermediates diffuse to the lithium anode and get reduced to short-chain (poly)sulfides, which either precipitate on lithium surface or shuttle back to the cathode. This parasitic reaction, called the polysulfide shuttling, continuously occurs in the cell (**Figure 1.2**). This process results in loss of active materials, accumulation of insulating layer on the lithium anode and rapid capacity fading. This is one of the major hurdles that limit the practical realization of the Li-S batteries. Others include low sulfur utilization rate (due to the extremely low conductivity of sulfur and Li_2S), high volume expansion during charging/discharging (2.03g cm^{-3} sulfur and 1.63g cm^{-3} Li_2S)[15].
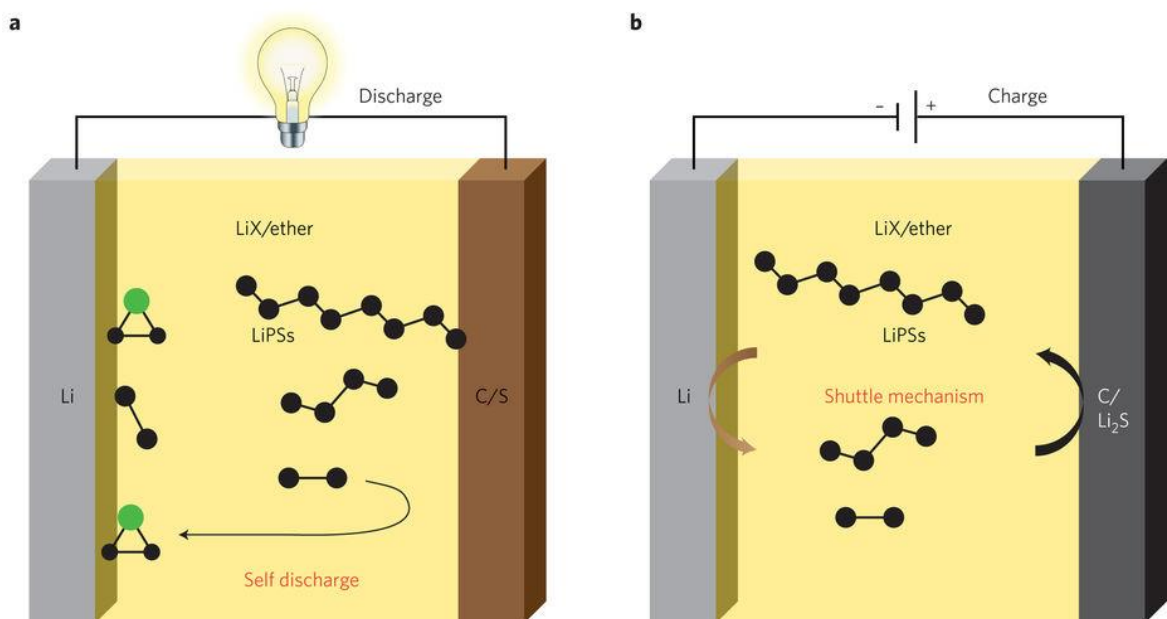
Figure 1.2: The configuration of a conventional Li-S battery using ether electrolytes and the fundamental problems with using porous carbons as a sulfur host material. Physical entrapment of sulfur/polysulfides in the positive electrode by porous carbons is not sufficient to prevent dissolution and diffusion into the electrolyte. a) During discharging, diffusion of soluble lithium polysulfides to the anode results in self-discharge via chemical reduction at the lithium surface, build-up of an insulating Li_2S/Li_2S_2 layer and loss of active material. b) During charging, redox shuttling of soluble lithium polysulfides between the electrodes gives rise to poor Coulombic efficiency and leads to precipitation of Li_2S at the exterior cathode surface. Stick-and-black ball structures represent long and short chain lithium polysulfides (Li_2S_8, Li_2S_4, Li_2S_2). LiX: electrolyte lithium salts. Reproduced from Ref. 14.

To solve the lithium polysulfides shuttling problem, much effort has been devoted to physical confinement of lithium polysulfides with carbonaceous materials[16,17,18,19,20,21] and host materials with strong chemical binding with lithium polysulfides[22,23,24,25,26,27]. These approaches can significantly increase the life time of lithium sulfur batteries. However, the protecting Li anode from dendrite formation and alleviating the consequent degradation and safety concern of organic electrolytes are another major challenge preventing the commercial applications of lithium sulfur batteries. All solid-state lithium batteries (ASSLBs), using solid electrolytes, are ideal candidates to solve these issues. Therefore, the development of novel solid electrolytes is urgent.

1.3 All Solid-State Lithium Batteries Overview

ASSLBs replace the traditional liquid electrolyte with a solid material. They are designed to not overheat or catch fire, as the solid electrolyte prevents dendrite growth.[28,29,30,31] There are two different types of ASSLBs: thin film (**Figure 1.3a**) and bulk (**Figure 1.3b**). The main difference between them is the thickness of electrodes and electrolyte: thin film cells are just several hundreds of nanometers thick, while bulk cells are several hundreds of micrometers thick. Typical thin film ASSLBs with $Li_{3.3}PO_{3.9}N_{0.17}$ (LiPON) as the solid electrolyte have already been commercialized with excellent performance.[32] However, it is only used in small scale applications which have low power demands, like smart cards and microelectronic devices. Furthermore, the fabrication of these batteries requires highly expensive vacuum deposition processes such as chemical vapor deposition, pulsed laser deposition. However, bulk-type ASSLBs are not only suitable for portable electronic devices, but also for large-scale energy storage system applications. One of the major advantages of bulk ASSLBs is that the

power and energy densities can be greatly enhanced by stacking the cells in series. Bulk solid electrolytes are usually prepared by mechanical milling, annealing, compaction, and heat-treatment. Electrodes are composed of active materials, solid electrolyte powders and electronic conductive materials, such as carbon, and they exist in a homogenous mixture as showed in **Figure 1.3b**.

1.3.1 Development of Solid-State Electrolytes

Solid electrolytes include a variety of materials like gels, polymers, organic–inorganic hybrids and inorganic materials. For the last 20 years, researchers have mainly focused on
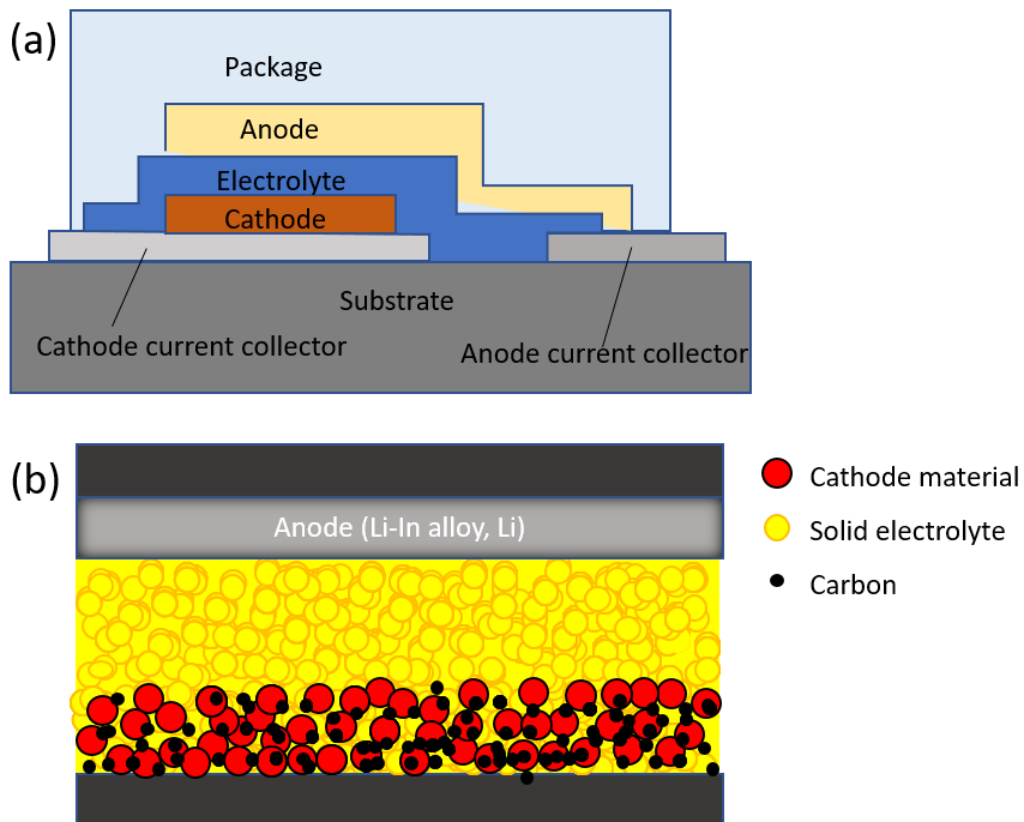
Figure 1.3: Schematic diagrams of (a) thin film-type battery and (b) bulk-type battery.

finding solid electrolyte materials with highly ionic conductivities, very low electronic conductivities, good chemical and thermal stabilities, and a wide electrochemical windows.[33] Until now, many solid electrolyte materials with conductivities between 10^{-4} - 10^{-2} S cm^{-1} at room temperature have been developed. Among these materials, oxides and sulfides are recognized as potential candidates for ASSLBs.[34]

In this proposal, inorganic solid electrolytes are discussed. Inorganic solid electrolytes can be divided into three categories: crystalline, glass and glass-ceramic. **Table 1.1** summarizes the ionic conductivities of typical oxide and sulfide solid electrolytes with ionic conductivities $\geq 10^{-4}$ S cm^{-1} at room temperature.

Table 1.1: Summary of various inorganic solid electrolytes with ionic conductivities $\geq 10^{-4}$ S cm^{-1} at room temperature.

Composition	Structure	Conductivity (S cm^{-1})	Reference
$Li_7La_3Zr_2O_{12}$	Crystal (garnet)	3×10^{-4}	Murugan et. al.[35]
$La_{0.51}Li_{0.34}TiO_{2.94}$	Crystal (perovskite)	1.4×10^{-3}	Itoh et al.[36]
$Li_{1.3}Al_{0.3}Ti_{1.7}(PO_4)_3$	Crystal (NASICON)	7×10^{-4}	Aono et. al.[37]
$Li_{1.07}Al_{0.69}Ti_{1.46}(PO_4)_3$ (LATP)	Glass-ceramic	1.3×10^{-3}	Fu et. al.[38]
$Li_{1.5}Al_{0.5}Ge_{1.5}(PO_4)_3$ (LAGP)	Glass-ceramic	4.0×10^{-4}	Fu et. al.[39]
$Li_{3.4}Si_{0.4}P_{0.6}S_4$	Crystal (thio-LISICON)	6.4×10^{-4}	Murayama et. al.[40]
$Li_{3.25}Ge_{0.25}P_{0.75}S_4$	Crystal (thio-LISICON)	2.2×10^{-3}	Kanno et. al.[41]
$Li_{3.25}P_{0.95}S_4$	Glass-ceramic	1.3×10^{-3}	Mizuno et. al.[42]
$Li_7P_3S_{11}$	Glass-ceramic	1.7×10^{-2}	Seino et. al.[43]
$Li_{10}GeP_2S_{12}$	Crystal	1.2×10^{-2}	Kamaya et. al.[44]
$Li_{10}SnP_2S_{12}$	Crystal	4×10^{-3}	Bron et. al.[45]
Li_6PS_5Cl (Argyrodite)	Crystal	1.3×10^{-3}	Boulineau et. al.[46]
$Li_{9.54}Si_{1.74}P_{1.44}S_{11.7}Cl_{0.3}$	Crystal	2.5×10^{-2}	Kato et. al.[47]
Li_4PS_4I	Crystal	1.2×10^{-4}	Sedlmaier et. al.[48]
$\beta\text{-}Li_3PS_4$	Crystal	1.6×10^{-4}	Liu et. al.[49]
$Li_7P_2S_8I$	Crystal	6.3×10^{-4}	Rangasamy et. al.[50]

1.3.2 Oxide Solid Electrolytes

Oxide electrolytes are typically ceramics, which have a high hardness and relatively good stability in air. Based on their structures, they can be further divided into four categories: LISICON, garnet, perovskite, and NASICON.

The LISICON structure solid electrolyte $Li_{14}Zn(GeO_4)_4$ was first developed in 1978 by Hong. It has a relatively low ionic conductivity 1×10^{-7} S cm^{-1} at room temperature.[51] Furthermore, this material is highly reactive with metallic Li and atmospheric CO_2 and the conductivity decreases with time.[33] So LISICON structure ionic conductors are not suitable as solid electrolytes.

Garnet structure materials have the general formula $Li_5La_3M_2O_{12}$ (M=Nb, Ta, Zr) and recently have been intensively studied as solid electrolytes. Compared to LISICON, they have higher ionic conductivities and excellent chemical stability with lithium metal. The cubic structure $Li_7La_3Zr_2O_{12}$ has a high ionic conductivity of 3×10^{-4} S cm^{-1},[35] and this can be further improved by substitution of Zr with other metals. For example, $Li_{6.5}La_3Zr_{1.75}Te_{0.25}O_{12}$ has the highest conductivity of 1.02×10^{-3} S cm^{-1}. However, high temperature sintering is necessary to achieve the garnet structure, and this dramatically complicates the battery fabrication process.

Perovskite solid electrolytes have the general formula ABO_3 with the structure of $CaTiO_3$. A series of $Li_{3x}La_{2/3-x}TiO_3$ has been synthesized with Li^+ ion conductivity exceeding 10^{-3} S cm^{-1} at room temperature.[36] The crystal structures of $Li_{3x}La_{2/3-x}TiO_3$ mainly depend on the compositions and preparation conditions; tetragonal, cubic or orthorhombic structures have been obtained. When it was synthesized by heating at 1350°C and then quenching, the lattice

was cubic; but when it was slowly cooled, the lattice was tetragonal or orthorhombic.[52] The conductivities of perovskites depend on the atoms in the A position, as Li^+ ions conduct from an A-site to the neighbouring A-site through a bottleneck diffusion channel surrounded by four oxygen atoms. Due to the attraction between Li^+ ions and O^{2-} ions, oxygen anions act as a potential barrier to conduction.[52] The high-valence La atom in the A position leads to A position vacancies and Li^+ ions transport by the vacancy mechanism. However, perovskite is not suitable as solid electrolytes, as they are unstable when in contact with Li metal. Ti^{4+} is easily reduced to Ti^{3+} by lithium metal.

NASICON compounds have the general formula $AM_2(PO_4)_3$, with the A site occupied by Li^+, Na^+ or K^+ and the M site occupied by Ge^{4+}, Ti^{4+} or Zr^{4+}. Among these materials, $LiTi_2(PO_4)_3$ has the highest ionic conductivity and has been extensively investigated.[33] Its ionic conductivity has been further improved by substituting M^{3+} for Ti^{4+} (M= Al, Cr, Ga, Fe, etc.). Among them, $Li_{1.5}Al_{0.5}Ge_{1.5}(PO_4)_3$ (LAGP) and $Li_{1.07}Al_{0.69}Ti_{1.46}(PO_4)_3$ (LATP) show the highest conductivities ($>10^{-4}$ S cm^{-1}).[38,39] Smaller Al^{3+} ions substitution decreases the unit cell parameters which leads to a better match of the size of the Li^+ ions and the diffusion channels.

In summary, NASICON-structure ionic conductors are considered suitable for high-voltage ASSLBs due to their high ionic conductivities at room temperature, good chemical stabilities and wide electrochemical windows. However, high temperature sintering and high interfacial ionic resistance has limited their practical use.

1.3.3 Sulfide Solid Electrolytes

Sulfide solid electrolytes have been developed over the past three decades. Researchers have mainly focused on their conductivities, chemical stabilities and mechanical properties. Sulfide solid electrolytes usually exhibit a high conductivity over 10^{-4} S cm^{-1}. However, they undergo decomposition as a result of hydrolysis once exposed to moisture in the air. Addition of other lithium salts can further increase their ionic conductivities and stabilities; they include lithium halides[50], lithium borohydride,[53] and lithium ortho-oxosalts[54].

Glassy sulfides had been studied extensively before any crystalline and glass-ceramic materials were reported. Glassy sulfide electrolytes generally show high conductivities and low activation energies due to the weaker bonding between lithium and sulfur anions in comparison with oxygen anions. Generally, glassy sulfide electrolytes exhibit conductivities in the range of 10^{-4}-10^{-3} S cm^{-1} at room temperature. Examples include $Li_2S \cdot P_2S_5$, [55] $Li_2S \cdot SiS_2 \cdot Li_3N$, [56] $Li_2S \cdot P_2S_5 \cdot LiI$, [57] $Li_2S \cdot SiS_2 \cdot LiI$, [58] $Li_2S \cdot SiS_2 \cdot Li_xMO_y$, [59] $Li_2S \cdot GeS_2$ [60] and $Li_2S \cdot B_2S_3 \cdot LiI$[61].

Glass-ceramics are partially crystalline materials prepared by crystallization of amorphous glasses by the heat treatment of glassy powders prepared by mechanical milling. They usually exhibit higher ionic conductivities than glassy sulfides as their grain boundary resistances are low due to the amorphous phases exist between crystalline materials, and their bulk conductivities are high. The class of compounds $xLi_2S \cdot (1-x) P_2S_5$ with x=0.7~0.8 has been extensively studied.[42,43] $Li_7P_3S_{11}$ and $Li_{3.25}P_{0.95}S_4$ are good examples of materials with ionic conductivities of 1.7×10^{-2} S/cm^{-1} and 1.3×10^{-3} S/cm^{-1} respectively. The ionic

conductivities of glass ceramic electrolytes were further improved by hot pressing the solid electrolytes, so that the grain boundary resistances were minimized by densification.[43] Glass ceramic solid electrolytes usually need lower heating temperatures (200-300°C) than crystalline materials. Crystalline solid electrolytes are always prepared at 450-600°C. The lower preparation temperatures make the ASSLBs fabrication processes easier.

Crystalline sulfide solid electrolytes usually have a thio-LISICON structure. In 2001, Kanno and coworkers reported a thio-LISICON $Li_{3.25}Ge_{0.25}P_{0.75}S_4$ phase superionic conductor.[42] This was the first crystalline ionic conductor with a high ionic conductivity of 2.2×10^{-3} S cm^{-1} at room temperature and a broad electrochemical window.[41] Then in 2011, the same group reported a new ionic conductor $Li_{10}GeP_2S_{12}$, which has an even higher ionic conductivity of 1.2×10^{-2} S cm^{-1} at room temperature. The extremely high conductivity attracted further research. Ceder and coworkers performed an *ab*-initio calculation of $Li_{10}GeP_2S_{12}$ that showed an ionic conductivity of 4×10^{-2} S cm^{-1} along the c-direction and 9×10^{-4} S cm^{-1} along the ab plane, with an overall conductivity of 9×10^{-3} S cm^{-1}.[62] This work suggests that ionic conduction in $Li_{10}GeP_2S_{12}$ occurs in three dimensions. As Ge is expensive, more recent work is focused on covalent substitution of Ge with Sn and Si.[45,47] $Li_{10}SnP_2S_{12}$ has been reported with an ionic conductivity of 4×10^{-3} S cm^{-1} which is slightly lower.[45] In 2016, $Li_{9.54}Si_{1.74}P_{1.44}S_{11.7}Cl_{0.3}$ was reported with the highest ionic conductivity of 2.5×10^{-2} S cm^{-1}.[47]

1.3.4 Comparison of Available Solid-State Electrolyte Materials

Even though ionic conductivity is the key factor for solid electrolytes, other properties such as wide electrochemical stability windows, good chemical compatibilities with electrode materials, excellent thermal and mechanical properties, simple preparation processes, low cost, easy integration and environmental friendliness are also important for practical applications. **Table 1.2** summarizes the comparison of available lithium ion conductive solid electrolyte materials. Oxide and sulfide solid electrolytes meet the requirements. Sulfide solid electrolytes have attracted more attention due to their high ionic conductivities, good mechanical properties, and wide electrochemical stability windows and selection of compositions. **Figure 1.4** shows the thermal evolution of ionic conductivity of the available solid-state electrolytes.[63] This clearly indicates that the ionic conductivities of some sulfide solid electrolyte materials have already exceeded the conductivities of traditional organic electrolytes (e.g. 1M Li_6PF_6 in EC/DMC/DEC) and they can also be used in high temperature all solid-state batteries. Despite the highly reactivity with moisture, they are still one of the most promising candidates for applications in ASSLBs, as they generally have high conductivities of over 10^{-4} S cm^{-1}, and the grain boundary resistances can be easily reduced by the cold pressing of sulfide electrolyte powders. Many researchers are still working on finding more stable sulfide solid ionic conductors. This proposal focuses on sulfide solid electrolyte materials.

Table 1.2: Comparison of lithium ion conductive solid electrolyte materials. Reproduced from Ref. 34.

Type	Materials	Conductivity (S cm^{-1})	Advantages	Disadvantages
Oxide	Perovskite, NASICON, LISICON, garnet	10^{-5}–10^{-3}	•High chemical and electrochemical stability •High mechanical strength •High electrochemical oxidation voltage	• Non-flexible •Expensive large-scale production
Sulfide	Li_2S-P_2S_5, Li_2S-P_2S_5-MS_x, Li_2S-P_2S_5-MS_x-LiX, Li_2S-P_2S_5-LiX (X = Cl, Br or I)	10^{-7}–10^{-3}	• High conductivity •Good mechanical strength and mechanical flexibility •Low grain-boundary resistance	•Low oxidation stability •Sensitive to moisture •Poor compatibility with cathode materials
Hydride	$LiBH_4$, $LiBH_4$-LiX, $LiBH_4$-$LiNH_2$, $LiNH_2$, Li_3AlH_6, Li_2NH	10^{-7}–10^{-4}	•Low grain-boundary resistance •Stable with lithium metal •Good mechanical strength and mechanical flexibility	•Sensitive to moisture •Poor compatibility with cathode materials
Halide	LiI, spinel Li_2ZnI_4, anti-perovskite Li_3OCl	10^{-8}–10^{-5}	•Stable with lithium metal •Good mechanical strength and mechanical flexibility	•Sensitive to moisture •Low oxidation voltage •Low conductivity
Thin-film	LiPON	10^{-6}	•Stable with lithium metal •Stable with cathode materials	•Expensive large-scale production
Polymer	PEO	10^{-4} at 65 - 78 °C	•Stable with lithium metal • Flexible •Easy to produce a large-area membrane • Low shear modulus	•Limited thermal stability •Low oxidation voltage (<4 V)
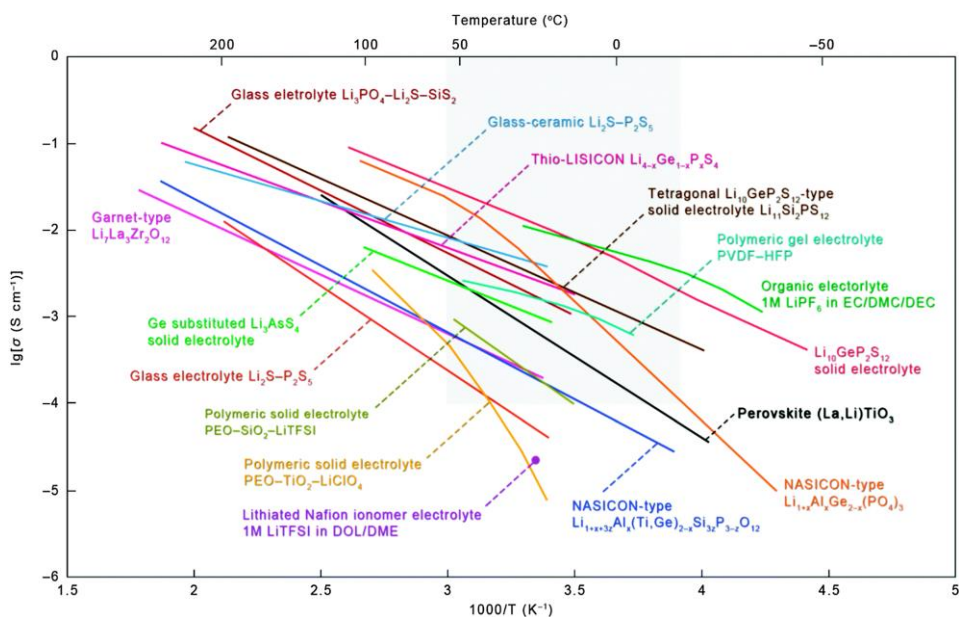
Figure 1.4: Arrhenius conductivity plots for solid electrolytes and traditional organic electrolytes. Reproduced from Ref. 39.

1.3.5 Challenges of Sulfide Solid Electrolytes

Classic solid state synthesis method

Despite the abovementioned issues, sulfide solid electrolyte materials have usually been synthesized by classic solid state high temperature reactions based on mechanical milling and sintering. Mechanical milling is high energy ball milling. Regarding the industrial production of solid electrolytes, this method is unfavorable in terms of costs and scale-up. Solvent-based soft chemistry synthesis methods have already been developed to synthesize these sulfide solid electrolytes. This will greatly decrease the cost and the process is easier to scale-up. Wet synthesis of Li_4PS_4I, β-Li_3PS_4, $Li_7P_2S_8I$ and $Li_7P_3S_{11}$ have been reported.[48,49,50,64]

In 2013, Liu and coworkers first reported the use of tetrahydrofuran (THF) as a reaction medium to synthesize nanoporous β-Li$_3$PS$_4$ with a high ionic conductivity of 1.6×10^{-4} S cm^{-1} at 25 °C.[49] In a typical synthesis, Li$_2$S and P$_2$S$_5$ with a stoichiometry of 3:1 were mixed in anhydrous THF at room temperature in an argon-filled glove box. The mixture was then stirred overnight and the white precipitate was collected by centrifugation and washed with THF three times. Finally, the material was heat treated to obtain the crystalline phase. **Figure 1.45a** shows the orthorhombic morphology of Li$_3$PS$_4$·3THF particles. **Figure 1.5b** indicates the same morphology and size of β-Li$_3$PS$_4$ as Li$_3$PS$_4$·3THF, and the high-resolution micrograph **Figure 1.5c** reveals the highly porous structure. β-Li$_3$PS$_4$ is only stable above 190°C and will be transformed to γ-Li$_3$PS$_4$ below 190°C. γ-Li$_3$PS$_4$ is a low ionic conductive phase. The paper concludes that the nanoporous structure leads to a high surface energy which induces a chemical lattice distortion that decreases the phase transition temperature and stabilizes the metastable β-Li$_3$PS$_4$ phase.
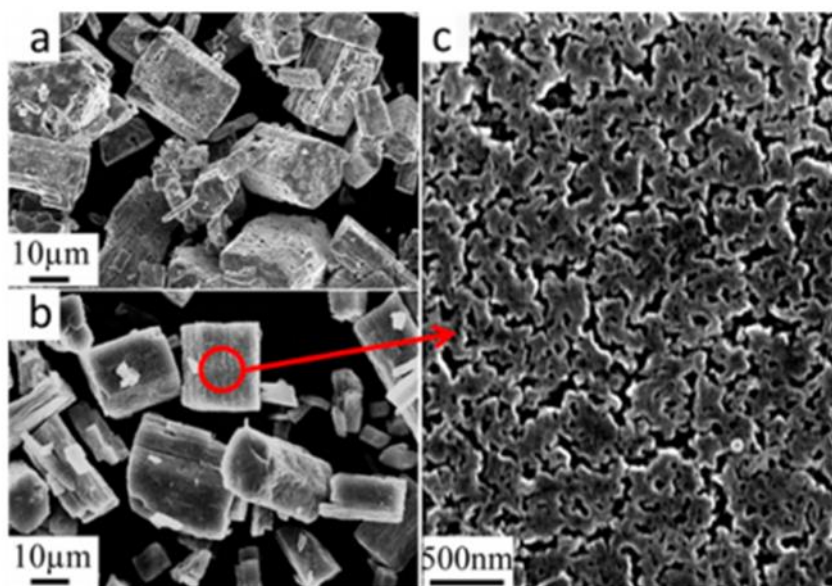
Figure 1.5: Characterization of porous structure. (a) Morphology of $Li_3PS_4\cdot 3THF$ particles synthesized by following the abovementioned procedures. (b) Morphology of nanoporous β-Li_3PS_4 particles. (c) Surface of the nanoporous β-Li_3PS_4.Reproduced from Ref. 49.

Later, Nobuya Machida's group successfully synthesized $Li_7P_3S_{11}$ solid electrolyte using 1,2-dimethoxyethane solvent (DME).[64] Similar to Liu's work, Li_2S and P_2S_5 were stirred for 3 days in DME at room temperature. Then DME was removed using a rotary evaporator. Finally, the sample was vacuum dried and heat treated to get the crystalline phase. The ionic conductivity of $Li_7P_3S_{11}$ synthesized with this wet synthesis method was reported as 2.7×10^{-4} S cm^{-1} at room temperature, which is slightly lower than traditional solid-state synthesis. This is caused by the lower crystallinity of the liquid synthesized phase; The impurities were presumed to be formed from the solvent, and the partially crystallized phase lowered the ionic conductivity.

In 2015, Liang's group reported using acetonitrile (ACN) to synthesize a new phase iodide-based $Li_7P_2S_8I$ superionic conductor.[50] The new phase exhibits the characteristics of a

solid solution between Li_3PS_4 and LiI with fast ion conduction and electrochemical stability up to 10V *vs* Li/Li^+. The authors suggested that the presence of iodide enhanced the stability of the electrolyte with the metallic Li anode. They showed results from different ratios of Li_3PS_4 and LiI reaction in ACN medium. A new phase formed at a 2:1 ratio and an excess of either phase led to a mixture of the excess phase and the newly formed phase showed in **Figure 1.6**. However, early this year, Jürgen Janek's group discovered a novel crystalline lithium superionic conductor Li_4PS_4I using a solvent-based synthesis approach.[48] Li_4PS_4I is synthesized by react Li_3PS_4 with LiI at the ratio of 1:1 in DME. This was the first crystalline thiophosphate in the quasi-ternary system Li_2S-P_2S_5-LiI. **Figure 1.7** shows its crystal structure compared to α-Li_3PS_4. Isolated PS_4^{3-} tetrahedra are arranged in layers perpendicular to the c-axis separated by I^- ions. The arrangement of the tetrahedra and their orientation are similar to α-Li_3PS_4. Li^+ ions diffuses in a 3D migration pathway with ionic conductivity around 1.2×10^{-4} S cm^{-1} at room temperature according to this report.
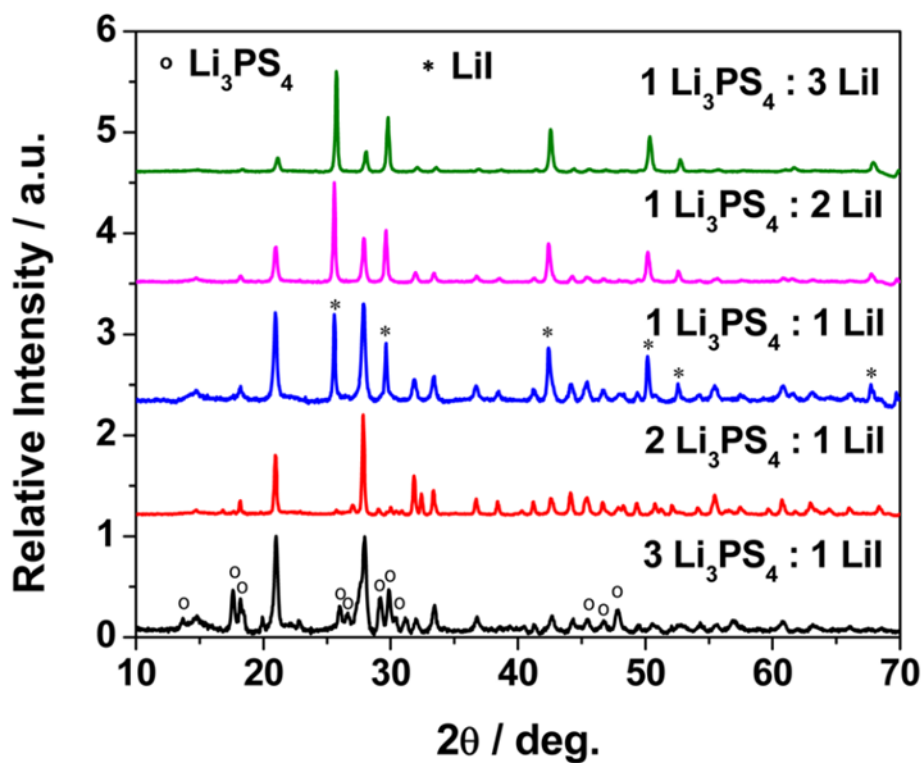
Figure 1.6: XRD data illustrating the formation of a new phase at the 2:1 stoichiometric composition of LPS: LiI. An excess of either phase leads to the observation of the respective phase as a secondary impurity in addition to the newly formed phase. Reproduced from Ref. 50.
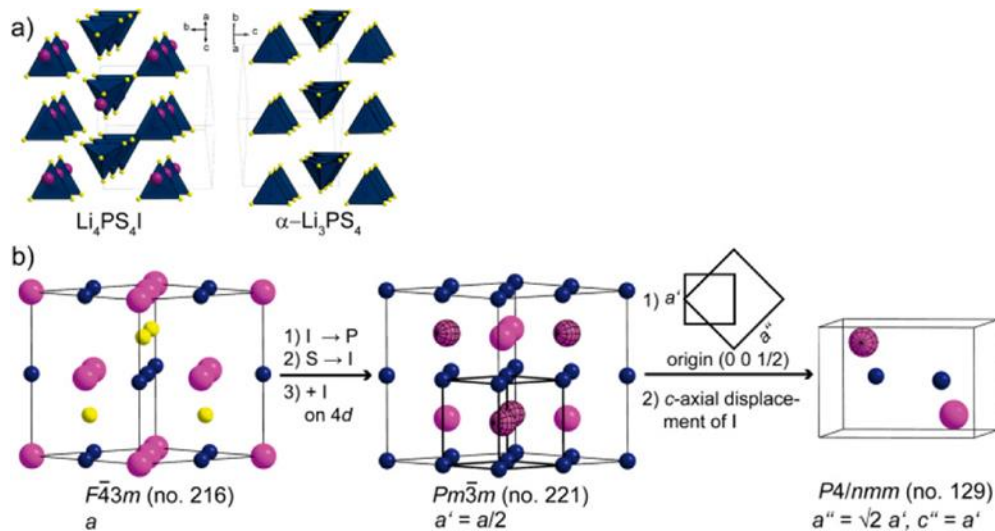
Figure 1.7: (a) Comparison of the tetrahedral arrangement of α-Li_3PS_4 with Li_4PS_4I where half of the tetrahedra are replaced by I^- (PS_4 tetrahedral, blue; I^-, purple; Li^+ ions); (b) structural derivation of the Li_4PS_4I structure from the argyrodite structure type (phosphorus, blue; I^-, purple; sulfur, yellow). Reproduced from Ref. 48.

Stability against lithium metal and cathode materials

Regardless of the progress in achieving high bulk conductivity, chemical incompatibility and electrochemical reaction play a role in degrading ASSLBs performance. It was predicated recently by density functional theory (DFT) calculation that most alkali solid electrolytes are thermodynamically not stable in contact with alkali metals and are reduced at low voltage with highly favorable decomposition energy (**Table 1.3** and **Figure 1.8**).[65] The lithiation and reduction of LGPS starts at 1.71 V vs Li/Li^+ and LGPS is eventually lithiated into $Li_{15}Ge_4$, Li_3P, Li_2S. Other sulfides materials are reduced at similar voltage 1.6-1.7 V to Li_2S, Li_3P, (LiCl, LiI, Li-Ge alloy).[65] Besides, the rate capability of most ASSLBs, particularly these using high-voltage oxide cathodes, remains poor.[66] This is due to high internal resistance
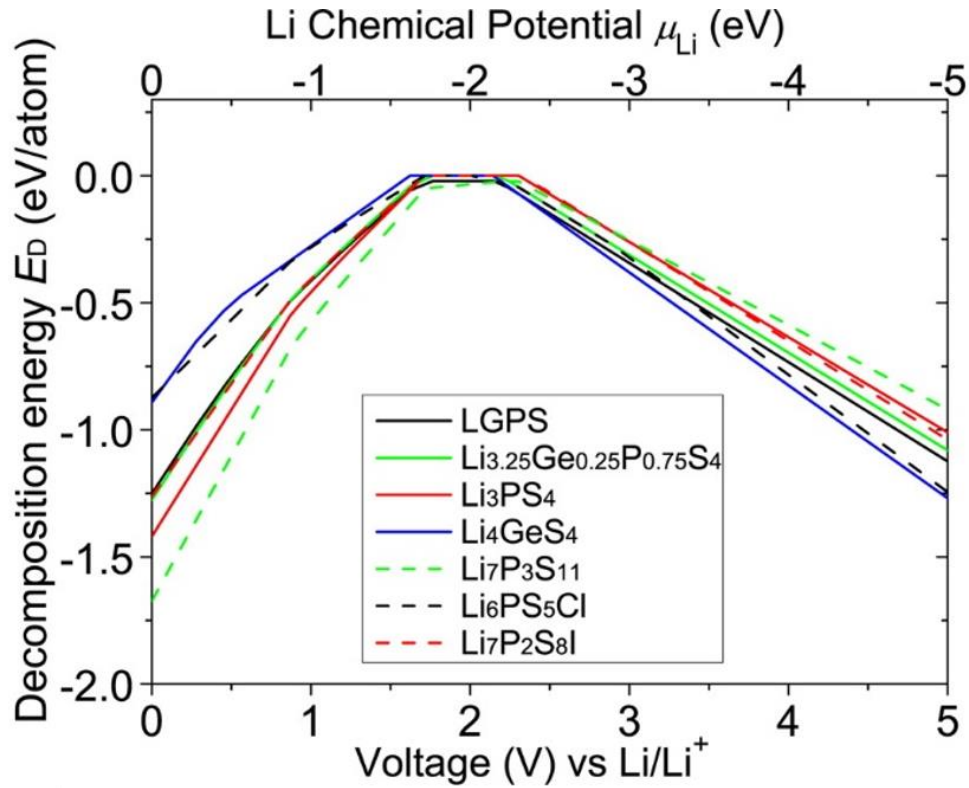
Figure 1.8: Decomposition energy E_D of sulfide solid electrolyte materials as a function of the applied voltage ϕ or Li chemical potential μ_{Li}. Reproduced from Ref. 65.

at the interface. Meanwhile with the use of high-voltage oxide cathode, sulfides solid electrolytes will be oxidized (the oxidation reactions of the solid electrolytes materials are summarized in **Table 1.4**).[65] The LGPS is delithiated and oxidized to P_2S_5, GeS_2 and S at 2.31V vs Li/Li$^+$. All other sulfide solid electrolytes are oxidized at 2-2.5V to form S, P_2S_5, (GeS_2). The oxidation reactions of sulfide solid electrolytes are highly favorable at 5V due to the low decomposition energy (**Table 1.4** and **Figure 1.8**).[65] Besides, sulfides solid electrolytes show less stable interfaces with cathode materials and the detailed reaction mechanisms were predicted by DFT calculation.[66] This suggests the bulk material stability or passivation by ionically conductive products at the cathode is essential to enhance the long term performance of ASSLBs.

Table 1.3: Reduction Reaction of the Solid Electrolyte Materials with Li Metal. Reproduced from Ref. 65.

	Phase equilibria with Li metal	E_D (eV/atom)
Li_2S	Li_2S (stable)	0
$Li_{10}GeP_2S_{12}$	$Li_{15}Ge_4$, Li_3P, Li_2S	-1.25
$Li_{3.25}Ge_{0.25}P_{0.75}S_4$	$Li_{15}Ge_4$, Li_3P, Li_2S	-1.28
Li_3PS_4	Li_3P, Li_2S	-1.42
Li_4GeS_4	$Li_{15}Ge_4$, Li_2S	-0.89
$Li_7P_3S_{11}$	Li_3P, Li_2S	-1.67
Li_6PS_5Cl	Li_3P, Li_2S, $LiCl$	-0.96
$Li_7P_2S_8I$	Li_3P, Li_2S, LiI	-1.26

Table 1.4: Oxidation Reaction of the Solid Electrolyte Materials at 5 V. reproduced from Ref. 65.

	Phase equilibria at 5 V	E_D (eV/atom)
Li_2S	S	-1.99
LGPS	GeS_2, P_2S_5, S	-1.22
$Li_{3.25}Ge_{0.25}P_{0.75}S_4$	P_2S_5, S, GeS_2	-1.08
Li_3PS_4	S, P_2S_5	-1.01
Li_4GeS_4	GeS_2, S	-1.27
$Li_7P_3S_{11}$	S, P_2S_5	-0.92
Li_6PS_5Cl	P_2S_5, S, PCl_3	-1.33
$Li_7P_2S_8I$	P_2S_5, S, I_2	-1.04
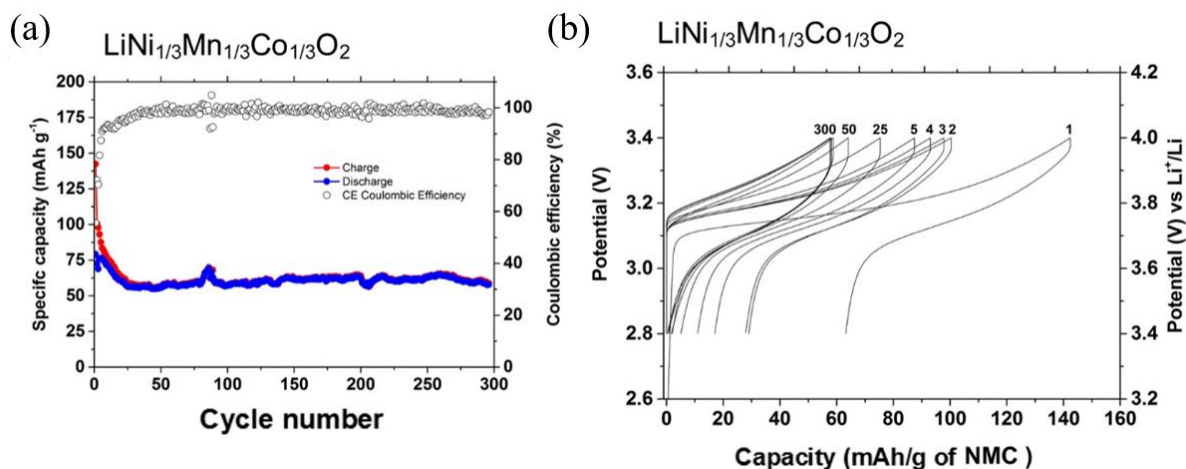
Figure 1.9: (a) Electrochemical behavior of NMC/Li$_6$PS$_5$Cl/Li–In Capacity retention vs cycle number and cycling efficiency. (b) Charge–discharge voltage profiles (only selected cycles are plotted). Reproduced from Ref. 67.

Rémi Dedryvère's group recently reported the interface stability of argyrodite Li$_6$PS$_5$Cl toward LiCoO$_2$, LiNi$_{1/3}$Co$_{1/3}$Mn$_{1/3}$O$_2$ and LiMnO$_4$ in bulk ASSLBs.[67] In this work, they focused on Li$_6$PS$_5$Cl to identify the reasons for capacity fading and to understand the interfacial reactivity for capacity fading and to understand the interfacial reactivity between argyrodite and active materials. ASSLBs LiCoO$_2$/Li$_6$PS$_5$Cl/Li-In, LiMn$_2$O$_4$/Li$_6$PS$_5$Cl/Li-In , and LiNi$_{1/3}$Co$_{1/3}$Mn$_{1/3}$O$_2$/Li$_6$PS$_5$Cl/Li-In were electrochemically cycled. XPS results show argyrodite is oxidized to elemental sulfur, lithium polysulfide, P$_2$S$_x$ (x≥5), phosphates, and LiCl at the interface with the positive electrodes materials.[67] However, these oxidation processes of the argyrodite solid electrolyte do not hinder the good cyclability of the battery because good capacity retention was observed over 300 cycles for the NMC/argyrodite/Li-In cells (**Figure 1.9**).[67] Additionally, the partial reversible formation of elemental sulfur and polysulfides shows the electrochemical activity of argyrodite, which contribute to the reversible capacity of the composite electrode.[67]

29

The interfacial reactivity and interphase growth of argyrodite solid electrolytes at lithium metal were reported by Juergen Janek group in 2017.[68] They used in situ X-ray photoemission technique combined with time-resolved impedance spectroscopy to investigate the thermodynamic stability against lithium metal. XPS results show Li_6PS_5X decomposes to an interphase composed of Li_3P, Li_2S and LiX in contact with lithium metal, which serves as an SEI and results in an increasing interfacial resistance.[68] Time-resolved impedance data of argyrodite solid electrolytes compared to $Li_7P_3S_{11}$ and $Li_{10}GeP_2S_{12}$ indicate Li_6PS_5Cl, Li_6PS_5Br and $Li_7P_3S_{11}$ exhibit nearly similar slow SEI formation, whereas Li_6PS_5I and $Li_{10}GeP_2S_{12}$ show much higher SEI resistance (**Figure 1.10**).[68] Reviewing the stability of the materials reported in this paper, $Li_7P_3S_{11}$ appears to be the most favorable material for application in ASSLBs.
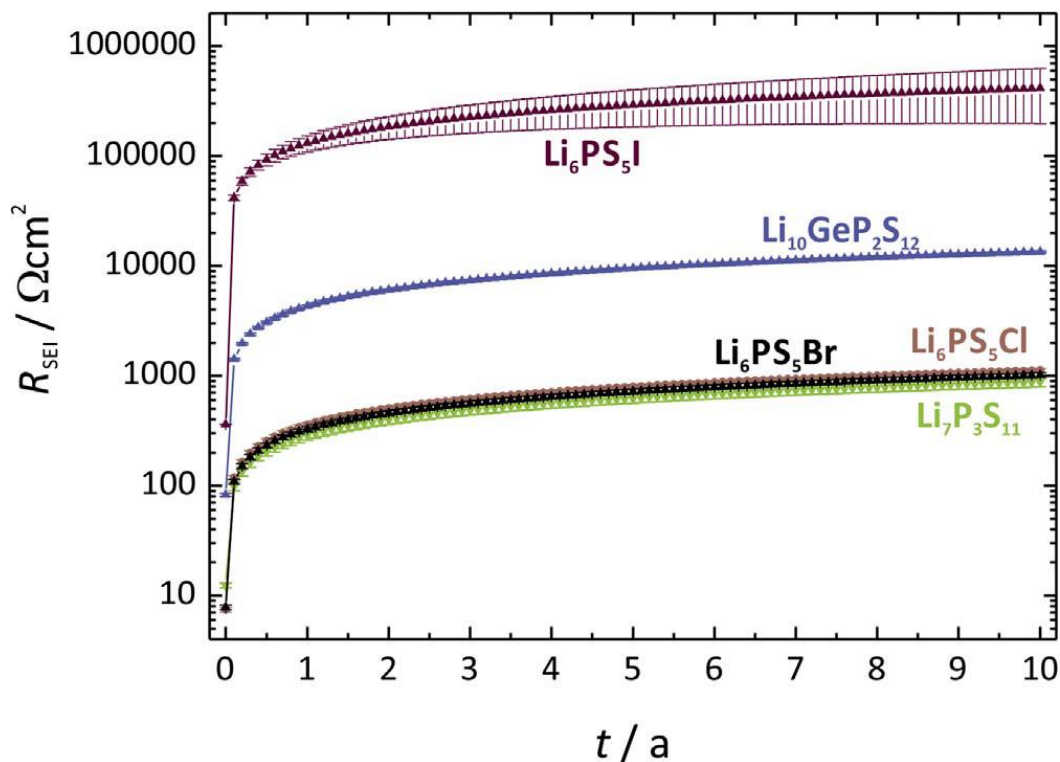
Figure 1.10: Simulation of the SEI resistance over 10 years for $Li_7P_3S_{11}$, $Li_{10}GeP_2S_{12}$, Li_6PS_5Cl, Li_6PS_5Br and Li_6PS_5I. reproduced from Ref. 68.

1.4 Summary

A variety of sulfide solid electrolytes with high ionic conductivity and low activation energy have been developed and partial conductivities have exceeded the traditionally organic electrolyte. However, the traditional high temperature solid state synthesis method, which is high cost and hard to scale up, greatly limits their applications in ASSLBs. Recently, wet synthesis of β-Li_3PS_4, $Li_7P_3S_{11}$, $Li_7P_2S_8I$ and Li_4PS_4I have been reported, which indicate the possibility of extending the method to other sulfide solid electrolytes. Besides, most sulfide solid electrolytes are thermodynamically not stable with lithium metals and chemical incompatible with cathode materials. A highly conductive sulfide solid electrolyte with high stability with lithium metal and good chemical compatibility with cathode materials is still under development. Different sulfide solid electrolytes have been predicted to satisfy the necessary combination of good phase stability, high lithium ion conductivity, wide band gap and good electrochemical stability based on DFT calculation. To accelerate the pace of all solid-state batteries' commercialization, the development of a simple and low cost wet synthesis method is urgent. Meanwhile, discovery of new sulfide solid electrolytes that is suitable for the applications in ASSLBs combined with different cathode materials is also a promising perceptive.

1.5 Scope of This Thesis

As discussed in the aforementioned introduction and summary (**chapter1**), it is essential to develop wet synthesis method of sulfide solid electrolytes and new sulfide solid electrolytes with high lithium ion conductivity and good stability with lithium metal and cathode materials. **Chapter 2** describes the characterization methods and techniques used in

this thesis. **Chapter 3** introduced the solvent-assisted synthesis of argyrodite Li_6PS_5X ($X=$ Cl, Br, I) solid electrolytes with high ionic conductivity and further improvement of ionic conductivities with antimony-doping. **Chapter 4** focuses on the synthesis of two potentially new sulfide solid electrolytes $Li_3Y(PS_4)_2$ and $Li_6Y_3(PS_4)_5$.

Chapter 2 Characterization methods and techniques

2.1 Materials Characterization

2.1.1 Powder X-ray Diffraction

X-ray diffraction (XRD) is the most commonly used technique to identify phase composition and to analyze crystal structure. Laue et. al. discovered in 1912 that X-ray with 0.01-10nm wavelength can be diffracted by the repeated atom planes, as it is in the same range as the atomic distance in a crystal. Bragg's law is used to explain the appearance of a unique diffraction pattern which identifies a specific structure, as showed in **Equation 2.1**.

$$n\,\lambda = 2\,d\,\sin\Theta \qquad\qquad \textbf{Equation 2.1}$$

where Θ is the angle between incident X-ray beam and the parallel planes, λ is the X-ray wavelength, and d represents the distance between crystallographic planes, as shown in **Figure 2.1**. The basic idea behind Bragg's law is that X-ray beams scattered from successive planes in the crystal will travel distance differing by exactly one wavelength (for the case of $n=1$). At the angle Θ, X-rays scattered from successive planes will interact constructively when they eventually reach the X-ray detector. As powder sample contains millions of single crystals that are oriented, diffraction beams are going towards all the directions obeying Bragg's law which results in the diffraction pattern. X-ray is actually scattered by the electron clouds around the atoms, the intensity of the diffraction beam directly correlates to the number and position of electrons. The intensity of the peaks is related to the structure factor (F) via the following **Equation 2.2**:

$I = A \cdot F^2$ **Equation 2.2**

Where *A* includes other factors such as polarization, absorption and temperature. Thus, the XRD pattern can be used to evaluate the crystal structure information.

XRD patterns in this thesis were collected using a PANalytical Empyrean with PIXcel^{3D} detector operating at 40 kV and 30mA with Cu K*a* (λ=0.15405 nm) radiation. Air

$1/2\lambda = d \cdot \sin \Theta$
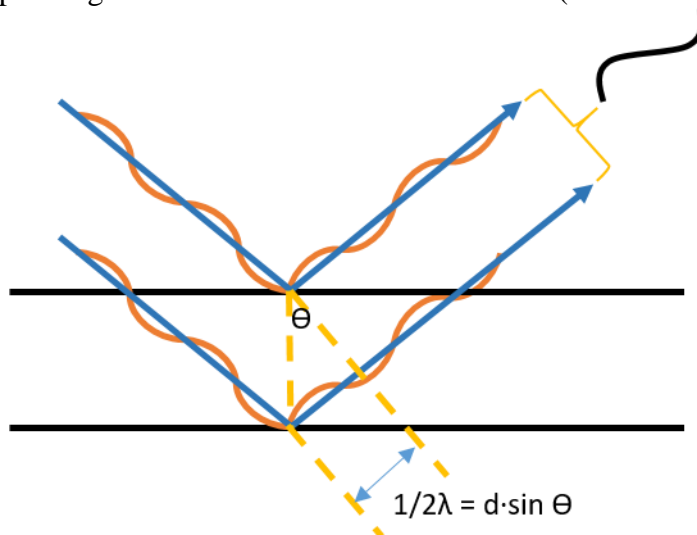
Figure 2.1: Schematic of Bragg's law.
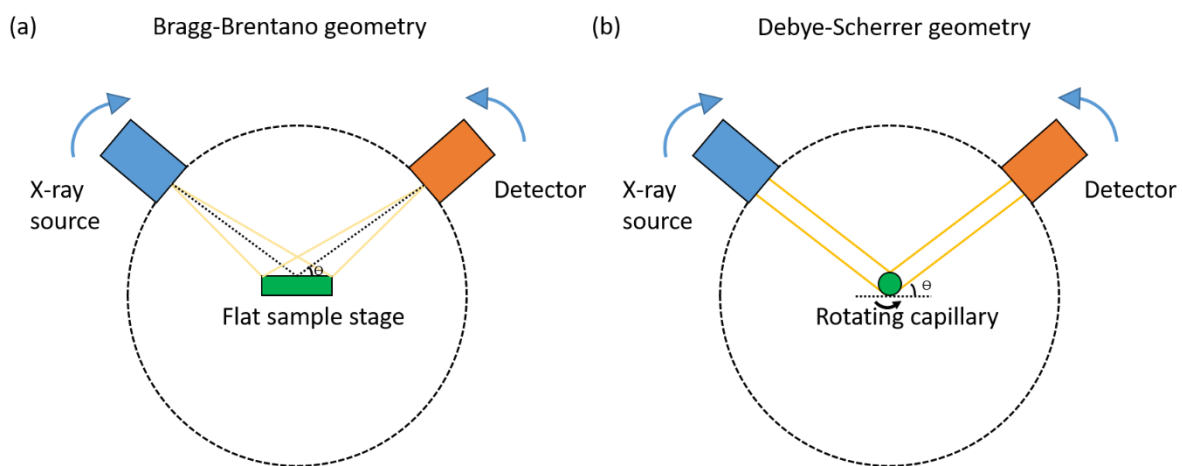
Figure 2.2: Schematic diagram of (a) Bragg-Brentano and (b) Debye-Scherrer geometries.

sensitive samples were applied on a silicon zero background holder and a protective Kapton film was sealed with vacuum grease on the top to allow X-ray penetration, while avoiding exposure to air during measurement. For overnight long scans, the powder samples were packed into glass capillary tubes (0.3mm diameter) sealed under Argon atmosphere with an acetylene oxygen torch. In this thesis, the Bragg-Brentano geometry (**Figure 2.2a**) were used for the short scans, long scans were conducted in Debye-Scherrer geometry (**Figure 2.2b**). Refinement of the XRD patterns were performed by using the software of GSAS II[69] and FullProf[70].

2.1.2 Scanning Electron Microscopy (SEM) and Energy Dispersive X-ray Spectroscopy (EDX)

SEM is used to visualize the micro/nanostructure morphology and the distribution of elements on the surface of a solid sample. In a typical SEM, a focused primary electron beam with an energy ranging from 0.2keV to 40keV hits the specimen surface, thus generating secondary electrons, backscattered electrons, transmitted electrons, and characteristic X-rays (fluorescence), as showed in **Figure 2.3**. They are detected by specialized detectors. Due to the repeated random scattering and absorption of primary electrons, their interaction with sample atoms only occurs within a certain depth which forms a teardrop shape. A few interactions would take place. Loosely bond electrons are ejected by collisions with incoming electrons and form secondary electron. Their energies are typically low, so they only occur near the surface of the specimen (~ 10 nm depth) and the deeper ones are absorbed on their way out. Meanwhile, the incident electrons are elastically scattered by the specimen. Those with a scattering angle >90° are called backscattered electrons (BSE). Heavier elements scatter

more strongly than lighter ones. Thus, the BSE provides information about atomic number and phase difference. With much larger energies than SE, deeper BSE (1~3μm depth) can also be measured. However, the spatial resolution of the BSE images is worse, due to the teardrop shape of the interaction volume. When a secondary electron is generated, a shell electron with relatively low binding energy is excited and leave an empty electron site behind. Consequently, one electron from outer shell will jump into the low energy empty site with the excessive energy released by emitting X-ray. The energy of the X-ray depends on the orbital energies involved and thus that is used for identifying element for EDX.

SEM images and EDX measurement in this thesis were carried out on a Zeiss Ultra Plus field emission SEM equipped with an EDX. Secondary electron mode was used for the purpose of imaging.
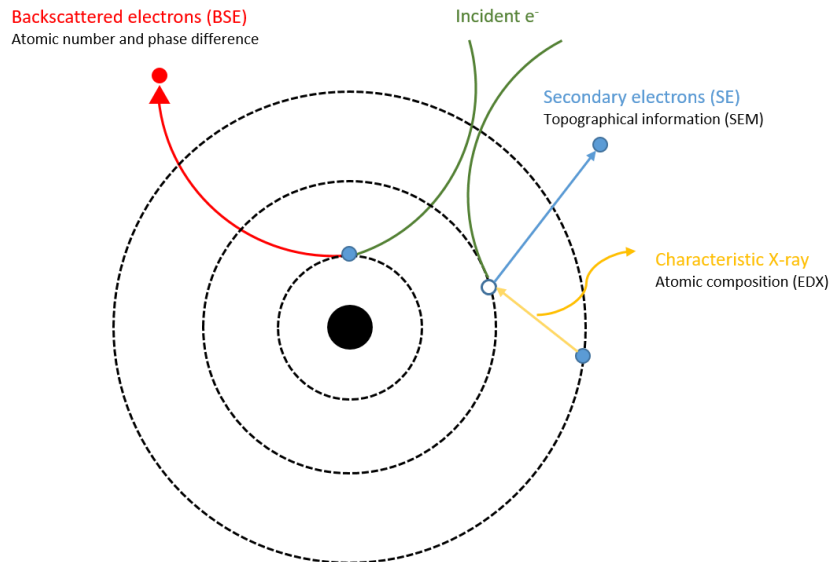
Figure 2.3: Schematic diagram of different types of interaction between the incident electron beam and specimen.

2.2 Electrochemical Techniques

2.2.1 Electrochemical Impedance Spectroscopy (EIS)

Impedance is a measure of the circuit characteristic to impede the flow of electrons through the circuit. Electrochemical impedance is normally measured by applying an AC potential to an electrochemical cell and the respond current through the cell is measured. Assume that a sinusoidal potential excitation is applied, the response to this potential is an AC current which can be analyzed as a sinusoid at the same frequency but shifted in phase. The excitation potential is usually small to ensure the cell's response is pseudo-linear. The expression of the impedance $Z(\omega)$ is presented in **Equation 2.3**.

$$Z(\omega)= E/I=Z_0 \exp (j\ \phi) =Z_0(\cos \phi + j \sin \phi) \qquad \textbf{Equation 2.3}$$

Where ω represents the radial frequency, ϕ is the shift in phase, $j = \sqrt{-1}$, and Z_0 is the amplitude of the impedance.

The expression of $Z(\omega)$ is composed of a real ($Z_0\cos \phi$) and an imaginary part ($Z_0\sin \phi$). Among various ways to present the data, the *Nyquist* plot is commonly used in the battery field by plotting the real part on X-axis and the imaginary part on Y-axis. The *Nyquist* plot usually consists of single or multiple arcs at high frequencies, followed by an inclined line at low frequencies. For the impedance measurements on a solid electrolyte, three semicircles correspond to resistance and capacitance of the bulk, the grain boundary resistance of the electrolyte, and the electrolyte/current collector interface will appear on the high frequencies and normally they form a single semicircle at room temperature at room temperature. The total impedance of the solid electrolyte is the sum of the three resistance abovementioned. And the

straight line at low frequencies corresponds to the overall electrolyte resistance. When the semicircle is not well defined in the measurements, especially for the low impedance sample, the resistance value can be extrapolation of the linear part to the X-axis.

In this thesis, EIS measurements were performed on VMP3 potentiostat/galvanostat station with EIS/Z capabilities (Bio-Logic). For EIS measurement, an AC voltage of 20-100 mV was applied with a frequency of 1000 kHz – 100 mHz.

2.2.2 Direct-Current (DC) Polarization

Direct current polarization is used to measure the electrical conductivity in ionic materials with ions as charge carriers. In this method, a constant DC potential is applied to a cell comprising of sample kept between two stainless steel electrodes and the resulting current is measured. After applying the DC potential, an interfacial polarization of mobile ions at the respective counter electrodes will quickly build-up, which result into a rapid increase in the resistance for mobile as time passes. The final stabilized current is then only corresponding to the electronic current. Based on the Ohm's law, the electronic conductivity can be expressed in **Equation 2.4**.

$$\sigma_{\text{electronic}} = \frac{I}{V} \times \frac{L}{A} \qquad\qquad \textbf{Equation 2.4}$$

where V and I are the applied voltage and measured current, L and A represent the thickness and the area of cross-section of the sample.

In this thesis, DC polarization measurements was conducted on VMP3 potentiostat/galvanostat station with EIS/Z capabilities (Bio-Logic). Three low potential 0.25V,

0.5V, and 0.75V was chosen in case of decomposing the electrolyte and each potential was

tested for 30 min in order to obtain a stabilized current.

Chapter 3 Solvent-assisted synthesis of Argyrodite Li₆PS₅X (X= Cl, Br, I) solid electrolytes with high ionic conductivity and Improvement of Li-ion conductivity in argyrodite solid electrolyte by antimony doping

3.1 Introduction

Over the past several years, various superionic Li-ion compounds have been investigated as candidates for lithium solid electrolytes.[71] Oxide materials are brittle and rigid which complicates their processing procedure in ASSBs. Problems arise with ensuring good interfacial contact with cathode and anode materials alike; accounting for volume expansion/contraction during cell cycling; and eliminating grain boundaries in solid electrolyte films at the anode. Conversely, sulfides are softer so that they are much more easily processed and densified.[72] Typical values for the Young's modulus for sulfides are in the range of 18-25 GPa[72], whereas values for oxides are usually higher than 150 GPa[73]. Meanwhile, some sulfide materials provide even higher ionic conductivities up to 10^{-2} S/cm, competitive with commercial liquid electrolytes. Among them, the argyrodite compounds show amongst the best stability against Li metal, with Li₂S, Li₃P and LiX (X= Cl, Br) formed at a slow rate when in contact with Li that acting as a protective passivating layer, as discussed in **Chapter 1**.[68] This has resulted in reports of a few pioneering ASSLBs that use Li-argyrodite as the solid electrolyte with different cathode and anode combinations (either Li foil or Li/In).[74,75,76,77,78,79,80]

3.2 Argyrodite Solid Electrolyte Li_6PS_5X

Argyrodite solid electrolytes have been extensively investigated owing to their high ionic conductivity and good stability against lithium metal and some lithium transition metal oxide cathode materials. The origin of the unusual high conductivity was investigated by using DFT molecular dynamics (MD) simulations.[81] Lithium vacancies and distribution of the halogens play an important role in lithium ion diffusion. The argyrodite Li_6PS_5X has a cubic unit cell in the $F-43m$ (No. 216) space group with ~10Å unit cell parameter. PS_4 groups centered at 4b sites build up the backbone, with remaining sulfur occupying 4a and 4d sites and lithium ions occupy the 48h sites surrounding the 4d sites. Halogens substituted sulfur occupy the 4a or 4d sites, whereas the sulfurs (16e) in the PS_4 groups are not substituted.[82] The lithium ions are distributed over the available 48h sites, with approximately 50% are occupied.[83] 48h sites exist in pair separated by only 1.9Å suggests each pair of 48h sites is occupied by one lithium ions.[83] Twelve 48h sites surrounded with 4d site, appear as a cagelik lithium ion structure. Besides the 48h site, lithium ion also occupy 24g sites in Li_6PS_5Br and Li_6PS_5I.[84] Between the 48h sites, three different types of jumps identified in MD simulations. The first type (doublet jump) is a jump between the paired 48h sites over a 1.9 Å distance. The second type (intracage jump) is the jumps within the cages between different 48h pairs over a distance of 2.25 Å. The third type (intercage jump) consists of the jumps interconnecting the four cages in each unit cell.[81] Three jump types must all occur in order to have lithium ion diffusion pathway and the smallest jump rate will limit macroscopic diffusion.

The lithium density during MD simulations is shown in **Figure 3.1** for Li_7PS_6, Li_6PS_5Cl and Li_6PS_5I.[81] There are only diffusion paths between the pairs of 48h sites are visible, thus the lithium ions in Li_6PS_5I only display local mobility, which explain its low rate of macroscopic lithium ion diffusion. In the other two, the regions with high lithium ion densities are connected to neighbouring high-density regions within a cage. Nevertheless, there is no clearly visible connection between different cages. In Li_6PS_5Cl, the lithium ion density is more spread out over the lithium ion positions, which indicates lithium ion are moving more rapidly inside the cages.[81]
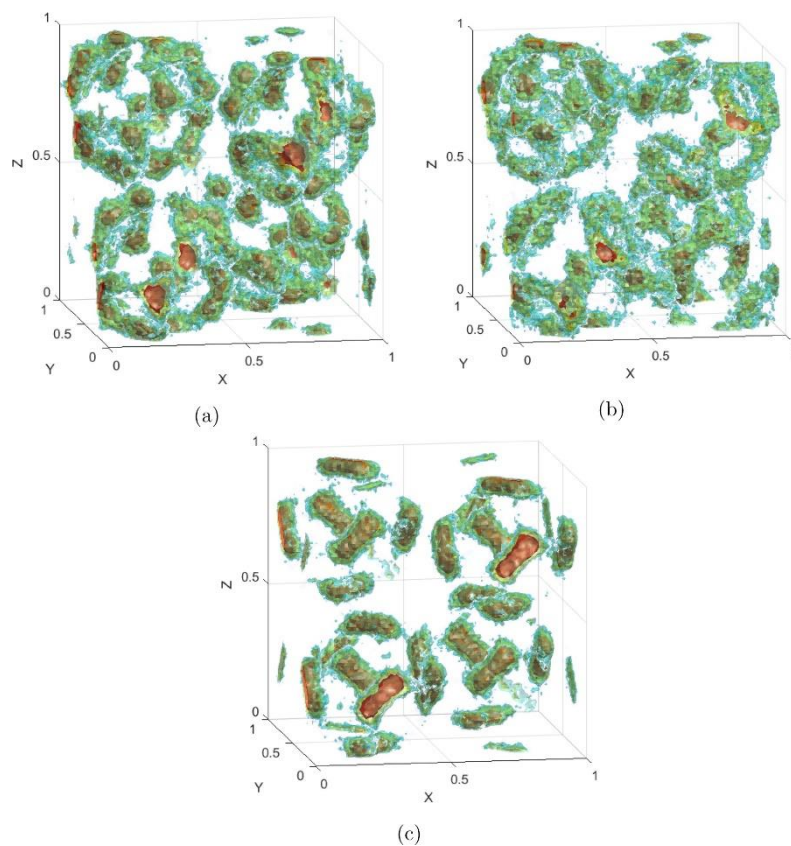
Figure 3.1: Li-ion density in the argyrodite unit cell during MD simulations at 450 K of (a) Li_7PS_6, (b) Li_6PS_5Cl, and (c) Li_6PS_5I. Red indicates high Li-ion density, followed by yellow, green, and blue representing lower densities. Reproduced from Ref. 81.

To investigate the large difference in macroscopic conductivity, the jump statistic was analyzed schematically, as showed in **Figure 3.2** for Li_7PS_6, Li_6PS_5Cl, and Li_6PS_5I.[81] In Li_6PS_5I, doublet jumps occur very frequently, in line with the lithium ion density result. Furthermore, only a few intracage jumps occur and no single intercage jump takes place during the MD simulation, thus revealing the reason of low conductivity Li_6PS_5I.[81] In all other compositions, doublet and intracage jumps occur frequently. However, only Li_6PS_5Cl and Li_6PS_5Br, a significant number of intercage jumps occur, which make macroscopic lithium ion diffusion possible.[81]

The explanation of the larger intercage jump rate in Li_6PS_5Cl is that replacing S^{2-} with Cl^- results in lithium ion vacancies that induce the higher lithium ion conductivity. It was proved by jump statistic simulations on the artificial Li_6PS_6 and Li_7PS_5Cl compositions.[81] As Li_6PS_6 has more vacancies, which should result in a high lithium ion conductivity by frequent intercage jumps. The decreased amount of vacancies in Li_7PS_6Cl should give rise to significantly fewer intercage jumps. Although Li_6PS_6 and Li_7PS_5Cl show significant differences in the intercage and doublet jump rates, the rate-limiting intercage jump are similar, as showed in **Figure 3.3**.[81] This indicates the Li-ion vacancies and substituting S^{2-} with Cl^- change the jump rate significant, which are responsible for highly ionic conductivity in Li_6PS_5Cl.

The impact of the halogen disorder explains the difference in conductivity between Li_6PS_5Cl and Li_6PS_5I. As I^- ions only occupy the 4a site, whereas Cl^- ions show disorder, being distributed over 4a and 4d sites.[83] To confirm it, the simulations were performed with different distribution of Cl^- ions over the 4a and 4d sites in Li_6PS_5Cl (**Figure 3.4**).[81] When all the Cl^- ions are located at 4a sites (similar to I^- ions in Li_6PS_5I), no intercage jumps occur during the MD simulation. If all Cl^- ions stay at the 4d sites, lithium diffusivity is also low due to the dramatically lower doublet jump rate. However, the intercage jump rate is greatly increased.[81]
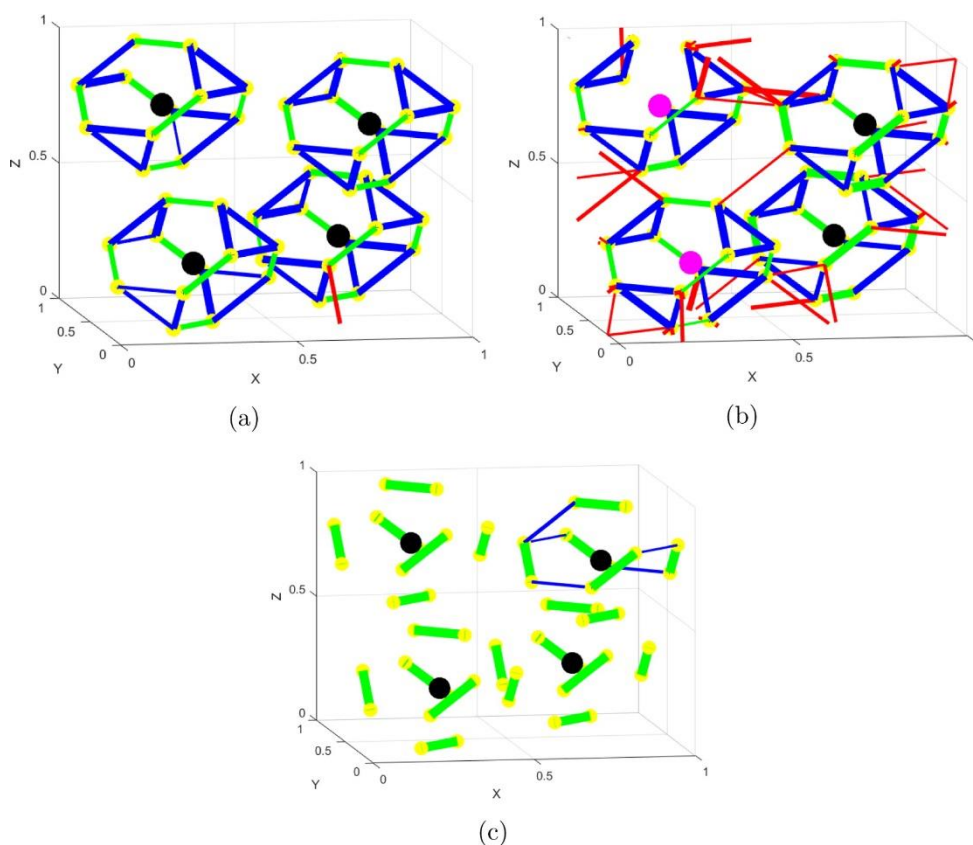
Figure 3.2: Jump statistic plots from MD simulations at 450 K of (a) Li_7PS_6, (b) Li_6PS_5Cl, and (c) Li_6PS_5I. The lines represent the three different types of jumps; green for doublet, blue for intracage, and red for intercage. Thicker lines represent larger jump rates. The colored spheres indicate S at site 4d (black), Cl at site 4d (pink), and Li-ion sites (48h) (yellow). Reproduced from Ref. 81.
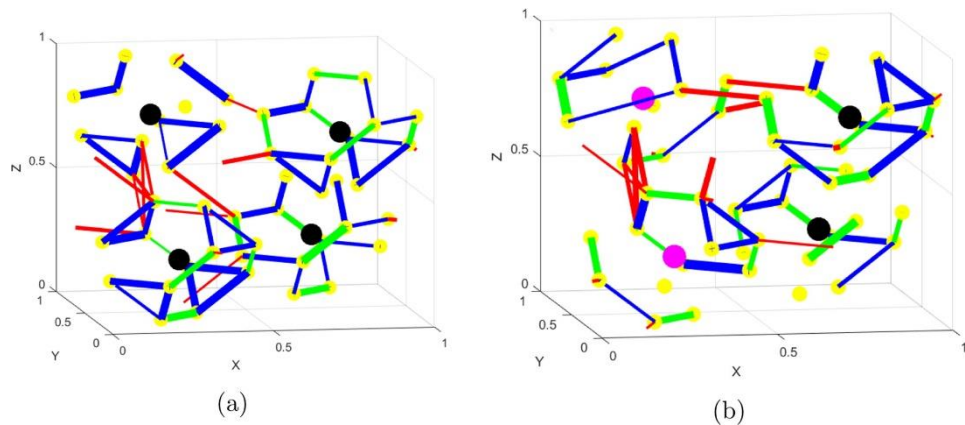
Figure 3.3: Jump statistic plots from MD simulations at 450 K of (a) Li_6PS_6 and (b) Li_7PS_5Cl. The lines represent the three different types of jumps; green for doublet, blue for intracage, and red for intercage. Thicker lines represent larger jump rates. The colored spheres indicate S at site 4d (black), Cl at site 4d (pink), and Li-ion sites (48h) (yellow). Reproduced from Ref. 81.
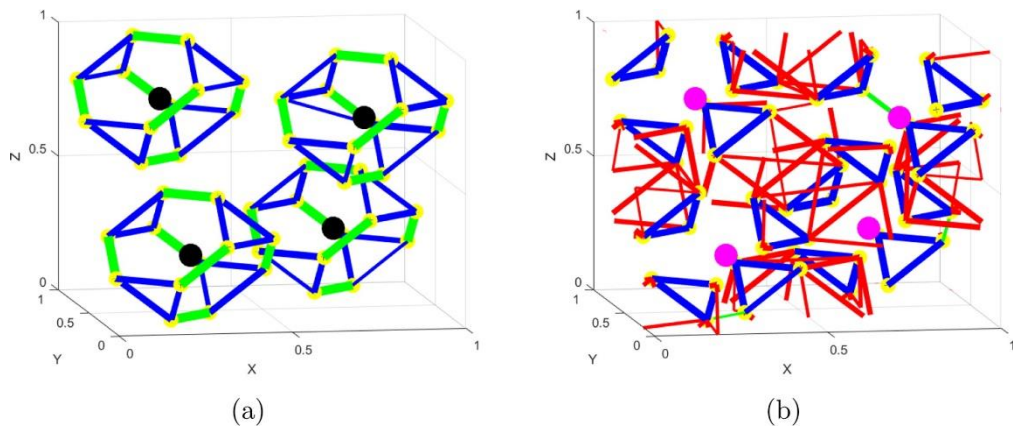
Figure 3.4: Jump statistic plots from MD simulations at 450 K of Li_6PS_5Cl with all chloride (a) on site 4a (outside the cages) and (b) on site 4d (inside the cages). The lines represent the three different types of jumps: green for doublet, blue for intracage, and red for intercage. Thicker lines represent larger jump rates. The colored spheres indicate S at site 4d (black), Cl at site 4d (pink), and Li-ion sites (48h) (yellow). Reproduced from Ref. 81.

3.3 Solvent-assisted synthesis of argyrodite Li_6PS_5X (X= Cl, Br, I) solid electrolytes with high ionic conductivity

This explains the origin of the argyrodites' high conductivity, more researchers are working on applying them in ASSLBs. Nevertheless, most Li-argyrodite electrolytes reported so far were synthesized by mechanical milling of the precursors followed by heat treatment. The ball milling process consumes much energy and makes the synthesis difficult to scale up. Solution-based synthesis, on the contrary, not only solves the above problems, but also provides a better mix of precursors, potentially reducing the subsequent heat treatment temperature and/or period. One attempt has been reported for the argyrodite Li_6PS_5Cl as well, involving a dissolution-reprecipitation process from an ethanol solution. However, a mechanical milling process was still required to obtain homogeneously mixed precursors, and the ionic conductivity of the product was only 1.4×10^{-5} S/cm, two magnitude orders lower than the materials obtained from a conventional all-solid-state process.[85] A direct "all solution" synthesis of the argyrodite Li_6PS_5X materials still remains a challenge to date.

Herein, I demonstrate a direct solution synthesis approach to argyrodite Li_6PS_5X (X = Cl, Br, I) solid electrolytes with high Li ion conductivities of $\sim10^{-3}$ S/cm at RT for the Cl and Br phases.

3.3.1 Synthesis and Characterization

In an Ar-filled glovebox, a stoichiometric 3:1 molar ratio of from Li_2S (Sigma-Aldrich, 99.98%) and P_2S_5 (Sigma-Aldrich, 99%) were mixed in a motor and dispersed in anhydrous tetrahydrofuran (THF). The mixture was stirred for 24 h at room temperature to obtain the β-

Li_3PS_4/THF suspension. The Li_2S (Sigma-Aldrich, 99.98%) and LiX (Sigma-Aldrich, >99%) with a molar ratio of 1:1 were dissolved in anhydrous ethanol, and the solution was added to the above suspension. The color of the mixture changed immediately after addition and the white precipitates dissolved gradually. After stirring overnight, the mixture was centrifuged at 8000 rpm for 10 min to remove the unreacted precipitates. The obtained clear solution was dried under vacuum, followed by to 150°C for 20 h in a Buchi oven to remove the solvents. Finally, the poorly crystallized powder was pressed into a pellet and annealed at 550°C for 6h with a ramping rate of 5°C/min to obtain the crystallized Li_6PS_5X product.

X-ray diffraction (XRD) measurements were conducted at room temperature on a PANalytical Empyrean diffractometer with Cu-Kα radiation equipped with a PIXcel bidimensional detector. XRD patterns for phase identification were obtained in the Bragg-Brentano geometry, with samples placed on a zero-background sample holder in an Ar-filled glovebox and protected by Kapton film (**Figure 3.5** patterns). Standard addition analysis was carried out by mixing the sample with 10 wt% Si in an Ar-filled glovebox and sealed in 0.3 mm glass capillaries. XRD patterns were collected in the Debye-Scherrer geometry (Figure 3.6 patterns).

The ionic conductivities were measured by the electrochemical impedance spectroscopy (EIS) with a home-built setup. Typically, 100 mg of the Li_6PS_5X powder was placed between two stainless steel rods and pressed into a 10 mm diameter pellet by a hydraulic press at 2T for 3 min in an Ar-filled glovebox. EIS was performed with 20 mV constant voltage within a frequency range of 1 MHz-10 mHz using the VMP3 potentiostat/galvanostat (Bio-logic). Direct-current (DC) polarization measurements were conducted on the same pellets

with applied voltages of 0.25 V, 0.5 V and 0.75 V for 30 min each to determine the electronic conductivities of samples.

3.3.2 Results and Discussion

Figure 3.5 shows the XRD patterns of the products after heat treatment. The argyrodite phase (*F*-43*m*) is present as the major crystalline phase (75 - 80%) for the Cl and Br argyrodites,
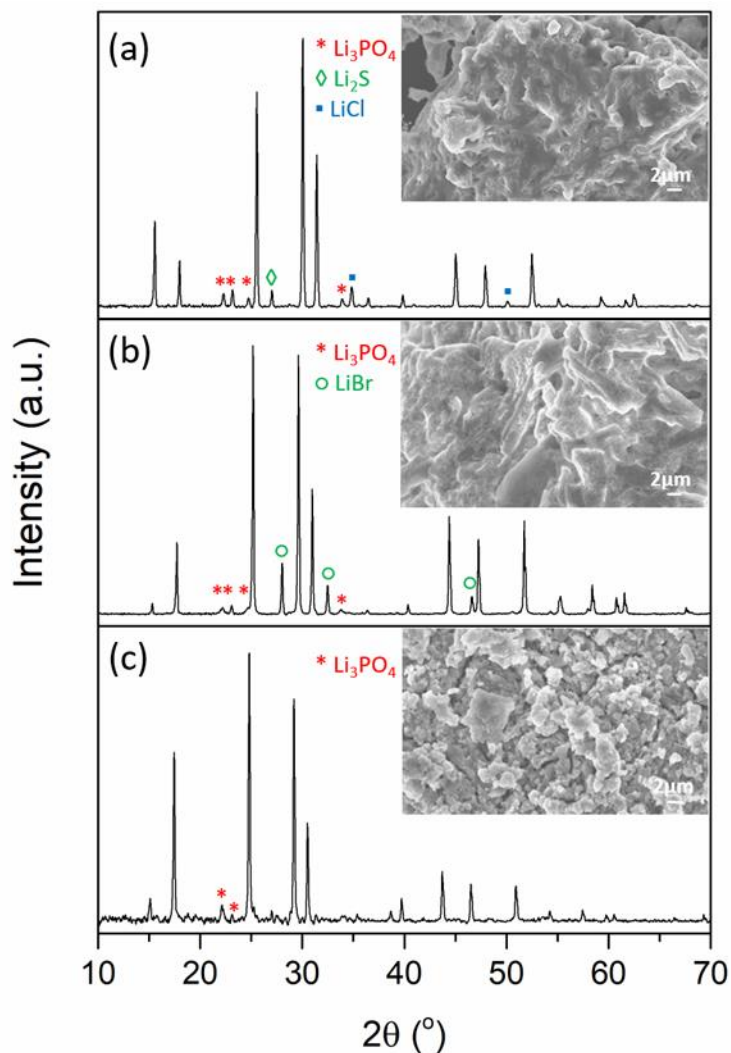
Figure 3.5: XRD patterns and SEM images (insets) of (a) Li_6PS_5Cl, (b) Li_6PS_5Br, (c) Li_6PS_5I from solution synthesis (all reflections correspond to the respective argyrodite phase except for the impurities as marked).

48

while the remainder is comprised of Li_3PO_4, LiCl/LiBr and Li_2S impurities. A similar solution synthesis procedure was also utilized to synthesize almost phase-pure Li_6PS_5I with only a trace of Li_3PO_4 impurity (**Figure 3.5c**). Despite the relatively low ionic conductivity of Li_6PS_5I, (**Figure 3.7c**) in agreement with previous reports,[86] this nonetheless demonstrates the broad application of this solution synthesis approach to the Li-argyrodite family.

An important factor for solid electrolytes is their degree of crystallinity. We determined the weight percent of the crystalline argyrodite phase in the products using Si as an external standard (see SI for details). Rietveld refinements[87] result in lattice and atomic parameters of Li_6PS_5Cl and Li_6PS_5Br similar to those previously reported values (**Figure 3.6**, **Table 3.1** and **Table 3.3**).[84] In the Li_6PS_5Cl and Li_6PS_5Br products, the weight percentages of crystalline argyrodite were 74(5)% and 81(5)%, respectively, with crystalline Li_3PO_4, LiX (Cl, Br respectively; about 7% of total fraction), and Li_2S impurities accounting for the remainder
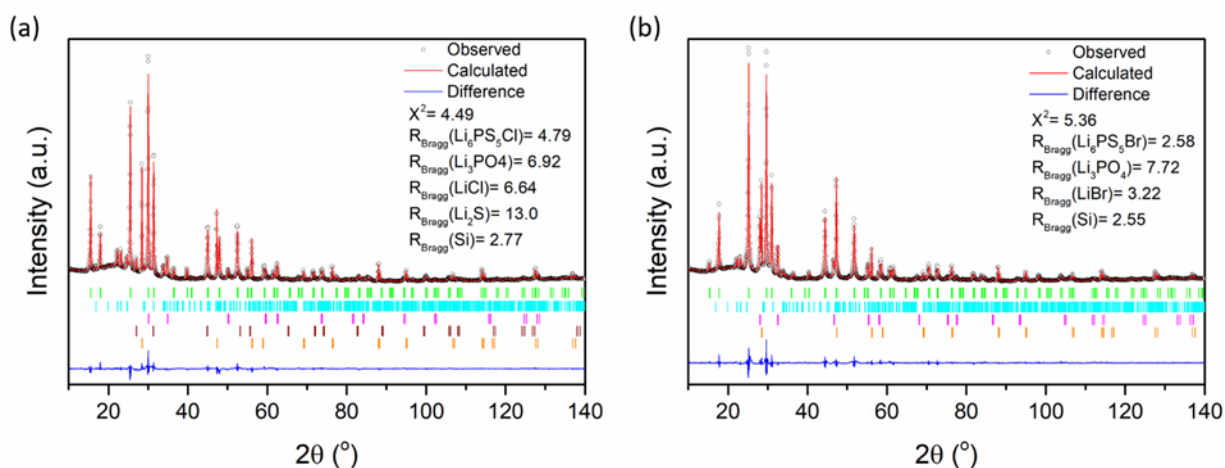
Figure 3.6: Rietveld refinement of XRD patterns of (a) Li_6PS_5Cl and (b) Li_6PS_5Br. Black crosses – experimental data; red lines – fitted data; blue lines – different curve between observed and calculated data; ticks – the Bragg peak positions of Li_6PS_5X (green), Li_3PO_4 (cyan), LiX (magenta), and Si (orange, 10 wt% addition).

(**Table 3** and **4**). The SEM images shown in **Figure 1a, b** (insets) of well-ground Li_6PS_5X (Cl, Br) materials illustrate the dense nature of the crystallite masses which are highly beneficial when the materials are processed into ASSBs. Highly ductile sulfide solid electrolytes have been shown to provide better contact at the grain boundaries than oxides, resulting in a more integrated solid electrolyte matrix, even in cold-pressed pellets without sintering.[43]

Table 3.1: Refined parameters for Li_6PS_5Cl (space group = F-43m, a = 9.8598(3) Å, R_{Bragg} = 4.79, X^2=4.49).

Atom	Wyckoff Site	x	y	z	Occ.	B_{iso} (Å^2)
Li1	48h	0.3221(2)	0.0040(4）	0.6779(2)	0.5	2
Cl1	4a	0	0	0	0.385	2.3(2)
Cl2	4d	0.75	0.75	0.75	0.615	2.3(2)
P1	4b	0	0	0.5	1	1.8(2)
S1	16e	0.1200(2)	-0.1200(2)	0.6200(2)	1	2.88(7)
S2	4a	0	0	0	0.615	2.3(2)
S3	4d	0.75	0.75	0.75	0.385	2.3(2)

Table 3.2: Weight fraction of each component in Li_6PS_5Cl (with ~10 wt% Si added as the reference standard for intensity normalization).

Component	Refined weight fraction with Si	Calculated weight fraction
Li_6PS_5Cl	65(2)%	74(5)%
Li_3PO_4	16(1)%	18(2)%
LiCl	7.6(4)%	8.6(8)%
Li_2S	2.2(3)%	2.5(5)%
Si	9.8(3)%	N/A

Table 3.3: Refined parameters for Li_6PS_5Br (space group = F-43m, a = 9.9855(4) Å, R_{Bragg} = 2.58, X^2 = 5.36).

Atom	Wyckoff Site	x	y	z	Occ.	B_{iso} (Å^2)
Li1	48h	0.3079(3)	-0.0103(6)	0.6921(4)	0.441	2
Li2	24g	0.25	-0.051(3)	0.75	0.119	2
Br1	4a	0	0	0	0.779(2)	2.8(2)
Br2	4d	0.75	0.75	0.75	0.221(2)	2.0(2)
P1	4b	1	0.5	1	1	1.6(2)
S1	16e	0.1185(2)	-0.1185(2)	0.6185(2)	1	2.45(9)
S2	4a	0	0	0	0.221(2)	2.8(2)
S3	4d	0.75	0.75	0.75	0.779(2)	2.0(2)

Table 3.4: Weight fraction of each component in the Li_6PS_5Br (with ~10 wt% Si added as the reference standard for intensity normalization)**.**

Component	Refined weight fraction with Si	Calculated weight fraction
Li_6PS_5Br	70(2)%	81(5)%
Li_3PO_4	14(2)%	16(3)%
LiBr	6.1(2)%	7.1(5)%
Si	9.6(3)%	N/A

The ionic conductivities of the solution-synthesized Li_6PS_5X solid electrolytes were measured by electrochemical impedance spectroscopy (EIS) in a SS/Li_6PS_5X/SS (SS=stainless steel) configuration at room temperature. Resistivities of 51 Ohm and 56 Ohm were obtained for Li_6PS_5Cl (**Figure 3.7a**) and Li_6PS_5Br (**Figure 3.7b**) at room temperature, converting to total conductivities of 2.0×10^{-3} S/cm and 1.4×10^{-3} S/cm, respectively. These values are in line
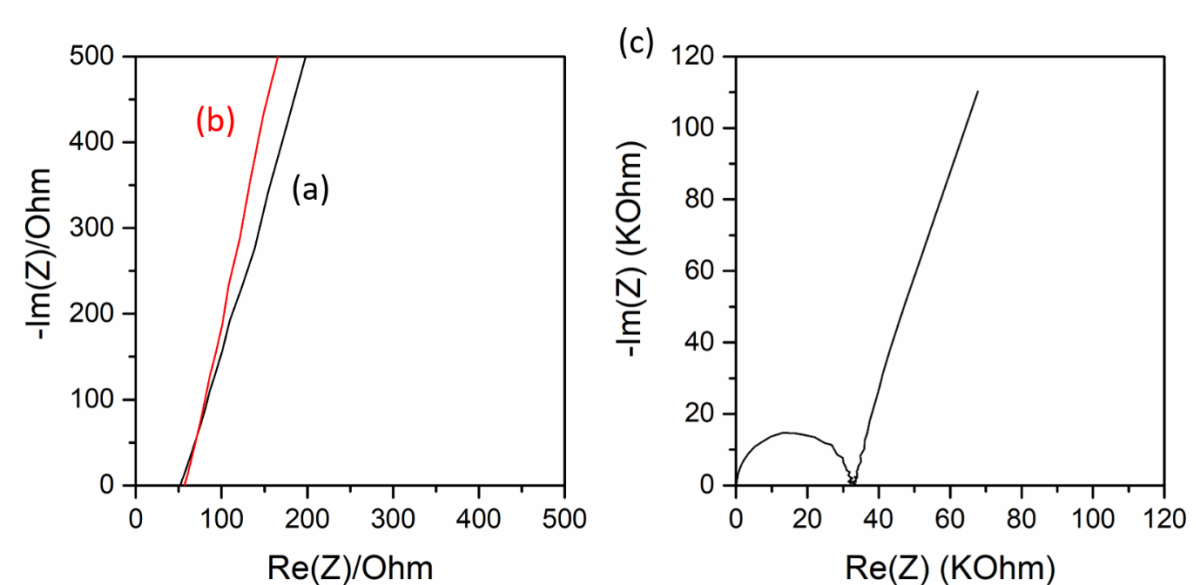
Figure 3.7: EIS plots for (a) Li_6PS_5Cl and (b) Li_6PS_5Br (c) Li_6PS_5Isolid electrolytes (cold-pressed at 2 T, measured at RT).

with values for solid state-synthesized argyrodites of 3×10^{-3} S/cm and 7×10^{-3} S/cm respectively. It also indicates that the impurities in the solution processed materials do not significantly lower the Li^+ conduction in the solid electrolyte. The ionic conductivity of the iodide argyrodite was 2×10^{-6} S/cm (**Fig. 3.7c**), in accord with the typically low values reported for this phase (i.e., 4×10^{-7} S/cm). The electronic conductivities of the two materials were measured by a DC polarization measurement of the SS/Li_6PS_5X/SS symmetric cells at room temperature.
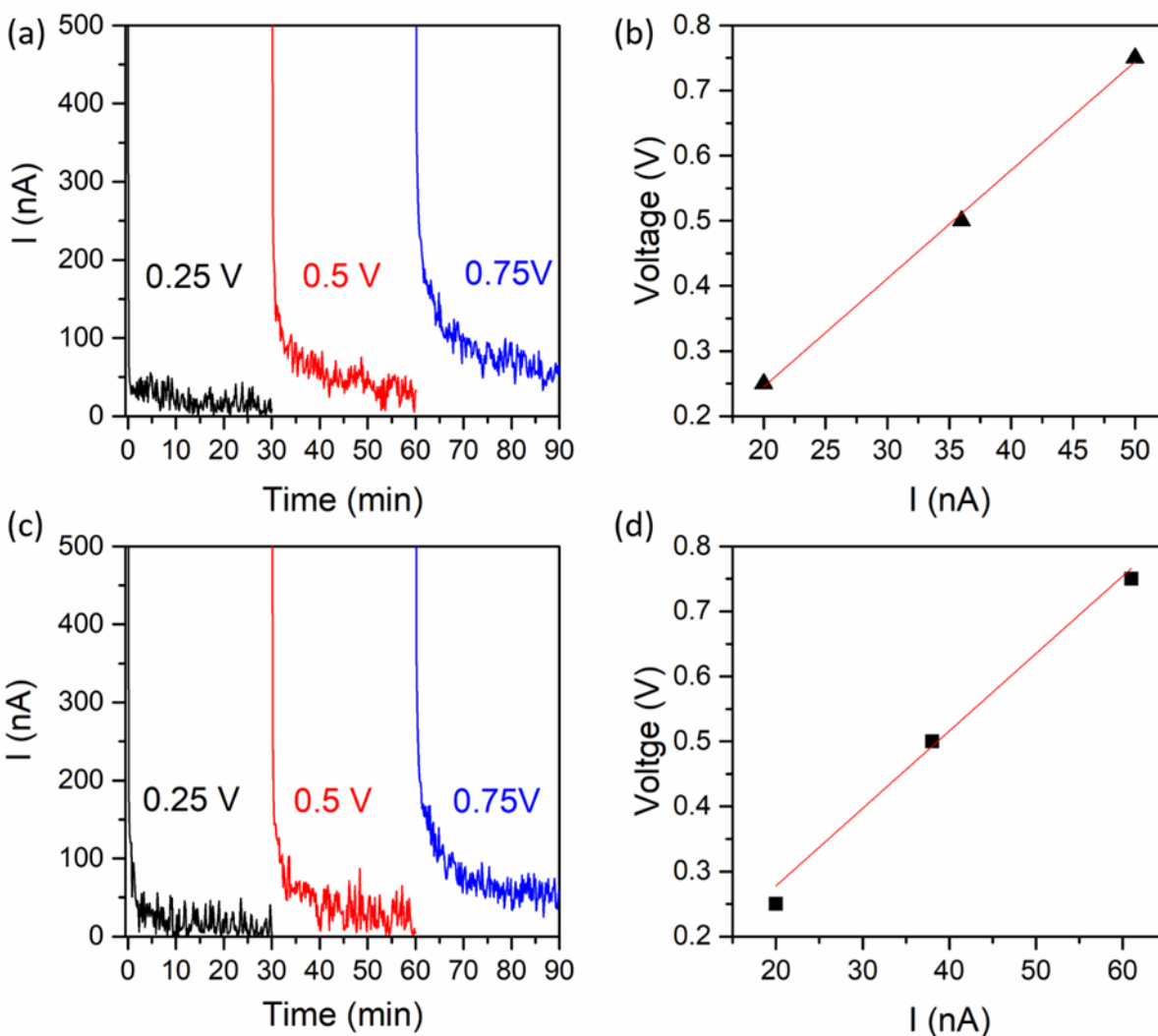
Figure 3.8: DC polarization curves of (a) Li_6PS_5Cl and (b) Li_6PS_5Br solid electrolytes with applied voltage 0.25V (black), 0.5V (red), 0.75V (blue). (b) and (d) are the linear fit.

53

Fig. 3.8 shows the DC polarization curves of Li_6PS_5Cl (**Fig. 3.8a**) and Li_6PS_5Br (**Fig. 3.8c**) at three voltages. After the initial 2 seconds, the current decays quickly and stabilizes at the order of 10^{-8} A after 30 min. From a linear fit of DC voltage and stabilized current (**Fig.3.8b** and **3.8d**), the DC electronic conductivities are estimated to be 5.1×10^{-9} S/cm for Li_6PS_5Cl and 4.4×10^{-9} S/cm for Li_6PS_5Br, both of which are 6 orders of magnitude lower than the ionic conductivities. This demonstrates that the argyrodite Li_6PS_5Cl and Li_6PS_5Br solid electrolytes obtained from solution synthesis are pure ionic conductors.

3.3.3 Summary

In summary, I developed a promising direct solution synthesis approach to argyrodite phases Li_6PS_5X (X = Cl, Br) by using THF/ethanol mixtures as the solvate. The resulting solid electrolytes show high ionic conductivities up to 2×10^{-3} S/cm and negligible electronic conductivities, in agreement with the argyrodites obtained from all-solid-state methods. Fully crystallized Li_6PS_5Cl and Li_6PS_5Br contribute to the high Li^+ conductivity. The soft and flexible sulfide solid electrolytes should allow excellent interfacial contact within the electrolyte as well as with the electrodes containing active cathode materials when they are assembled into full cells. The solution synthesis present in this work is scalable and can be applied to related compounds by varying the solvent selection, i.e., DME/ethanol or simply ethanol. At the same time, the approach allows intimate ionic contact between electrolyte and electrodes through a simple solution coating method, providing further improvement of the electrochemical performance of all-solid-state batteries. We believe that our results provide new insight into simple synthesis of already existing as well as new halide-thiophosphate solid electrolytes.

3.4 Improvement of Li-ion conductivity in argyrodite solid electrolyte by antimony-doping

As discussed in **Chapter 3.2**, replacing sulfur with halogen introduces lithium vacancies, the distribution of the halogens over the available sites is equally important. The halogen distribution determines the distribution of lithium vacancies. I^- has bigger size resulting in that it cannot enter into 4d sites and orders in 4a sites, which dramatically decreases the conductivity of Li_6PS_5I. Besides, it was reported that the Li-ion conductivity of Li_6PO_5Cl and Li_6PO_5Br was around 10^{-9} S/cm due to the 20% smaller lattice constants that dramatically reduce the free volume for Li-ion diffusion.[88]

In this study, I focus on improving the Li-ion conductivity of argyrodite Li_6PS_5X with antimony doping to increase the unit cell volume which may introduce I^- ion disorder over 4a and 4d sites in Li_6PS_5I and enlarge the diffusion pathway to further improve the ionic conductivities in argyrodites.

3.4.1 Synthesis and Characterization

Li_2S (Sigma Aldrich 99.98%), P_2S_5 (Sigma Aldrich 99%), Sb_2S_3 (Sigma Aldrich 99.995%%), sulfur (Sigma Aldrich $\geq$99.5%), and LiX (X=Cl, Br, I) (Sigma Aldrich >99%) were used as starting materials and mixed in stoichiometric proportions to yield global compositions of $Li_6Sb_yP_{1-y}S_5X$ inside an argon filled glovebox. The powder after ground were then cold pressed (1g) at 2 tons into 13mm diameter pellets. The pellets were then transferred into carbon coated quartz tubes and sealed under vacuum. Finally, the samples were crystallized at 550°C for 100 h with a ramping rate 5 °C/min.

X-ray diffraction (XRD) measurements were conducted at room temperature on a PANalytical Empyrean diffractometer with Cu-Kα radiation equipped with a PIXcel bidimensional detector. XRD patterns for phase identification were obtained in the Bragg-Brentano geometry, with samples placed on a zero-background sample holder in an Ar-filled glovebox and protected by Kapton film.

The ionic conductivities were measured by the electrochemical impedance spectroscopy (EIS) with a home-built setup. Typically, 100 mg of the glass ceramic Li_6PS_5X powder was placed between two stainless steel rods and pressed into a 10 mm diameter pellet by a hydraulic press at 2T for 3 min in an Ar-filled glovebox. EIS was performed with 20 mV constant voltage within a frequency range of 1 MHz-10 mHz using the VMP3 potentiostat/galvanostat (Bio-logic).

3.4.2 Results and Discussion

Figure 3.9 shows the XRD patterns of $Li_6Sb_yP_{1-y}S_5I$ (y=0.1, 0.3, 0.5, 0.8, 1.0) after heat treatment. $Li_6Sb_{0.1}P_{0.9}S_5I$, $Li_6Sb_{0.3}P_{0.7}S_5I$ and $Li_6Sb_{0.5}P_{0.5}S_5I$ shows nearly phase pure patterns which correspond to the argyrodite (F-43m) and peaks are continually shifting to the left (low theta)) compared to the argyrodite Li_6PS_5I as showed in **Figure 3.10**. Due to the larger ionic size of Sb^{5+} than P^{5+}. Left shifted (low theta) peaks means lager unit cell volume. For the XRD pattern of $Li_6Sb_{0.8}P_{0.2}S_5I$, it consisted of larger left shifted (low theta) argyrodite peaks compared to $Li_6Sb_{0.5}P_{0.5}S_5I$ which indicated that possible higher content Sb doping (y>0.5) is possible and a series of unknown phase peaks. In the Li_6SbS_5I pattern, a mix of different

56
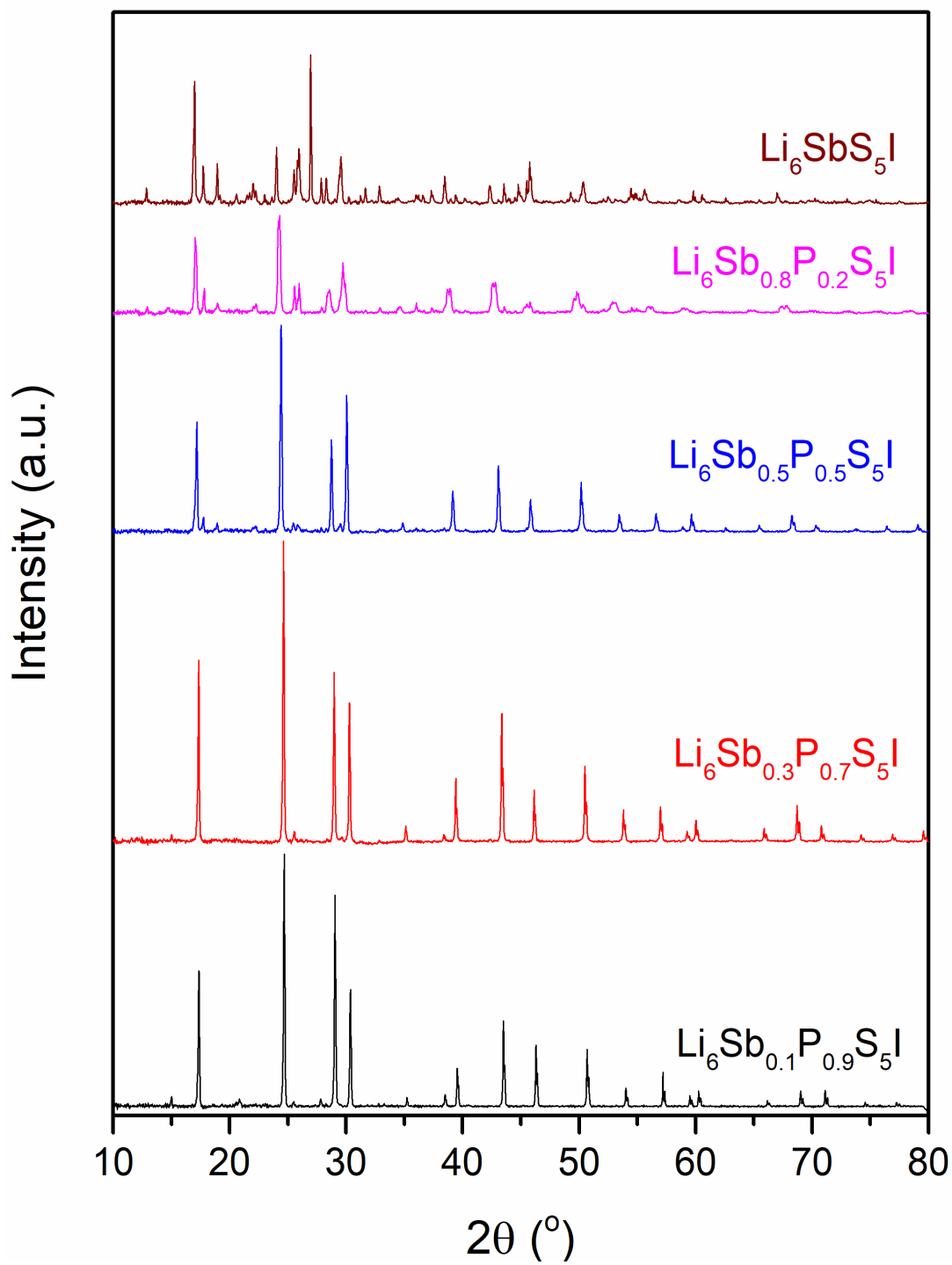
Figure 3.9: XRD patterns of $Li_6Sb_yP_{1-y}S_5I$ (y=0.1~1), heat treated at 550^oC for 100h with an ramping rate $5^oC/min$.

unknown peaks were observed. Nevertheless, after heat treatment, with high content of Sb, the samples start to melt ($Li_6Sb_{0.8}P_{0.2}S_5I$ and Li_6SbS_5I) and react with the quartz tube (Li_6SbS_5I). Possible lower temperature heat treatment will give phase pure $Li_6Sb_{0.8}P_{0.2}S_5I$ and Li_6SbS_5I. Besides, the reported air stable Na_3SbS_4 with SbS_4 unit indicate the possibility of phase pure Li_6SbS_5I and increasing the air stability of $Li_6Sb_yP_{1-y}S_5X$ with antimony doping.

The ionic conductivities of the as-synthesized $Li_6Sb_yP_{1-y}S_5I$ solid electrolytes were measured by EIS in a $SS/Li_6Sb_yP_{1-y}S_5I/SS$ (SS=stainless steel) configuration at room temperature, listed in **Table 3.5**. Sb doped Li_6PS_5I shows higher conductivities than the non-

Figure 3.10: Comparison of the XRD patterns of as-synthesized $Li_6Sb_yP_{1-y}S_5I$ with argyrodite Li_6PS_5I (ICSD #418489).

doped Li_6PS_5I with no clear regularity. As the ionic conductivity are highly depending on the synthesis parameters and measurement conditions, further repeated experiment and lower temperature heat treatment will be performed to ensure no measurement errors and find the ionic conductivity increasing regularity.

Table 3.5: Li-ion conductivities of $Li_6Sb_yP_{1-y}S_5I$ compared to Li_6PS_5I (Reported value).

Sample	Conductivity
Li_6PS_5I	4×10^{-7} S/cm (Reported by Pecher *et. al.*[86])
$Li_6Sb_{0.1}P_{0.9}S_5I$	1.39×10^{-6} S/cm (This work)
$Li_6Sb_{0.3}P_{0.7}S_5I$	1.23×10^{-6} S/cm (This work)
$Li_6Sb_{0.5}P_{0.5}S_5I$	4.30×10^{-6} S/cm
$Li_6Sb_{0.8}P_{0.2}S_5I$	Not tested
Li_6SbS_5I	Not tested

As antimony can be successfully doped into argyrodite Li_6PS_5I, it may be also able to be dopes into the argyrodite Li_6PS_5Cl and increase the ionic conductivity. **Figure 3.11** shows the XRD patterns of $Li_6Sb_yP_{1-y}S_5Cl$. With 10% Sb doping, it forms the argyrodite phase with some small extra peaks corresponding to unknown phases. With the increasing amount of doped Sb (50% and 80%), the intensity of impurities phase peaks starts to increase and the intensity of the argyrodite peaks decreases which indicated high Sb doping will lead the argyrodite structure collapses. **Figure 3.12** shows the comparison of the as-synthesized $Li_6Sb_yP_{1-y}S_5Cl$ with argyrodite Li_6PS_5Cl (ICSD# 418490), which indicates no clear peaks shift. The ionic conductivities of $Li_6Sb_yP_{1-y}S_5Cl$ remain around 10^{-3} S/cm.

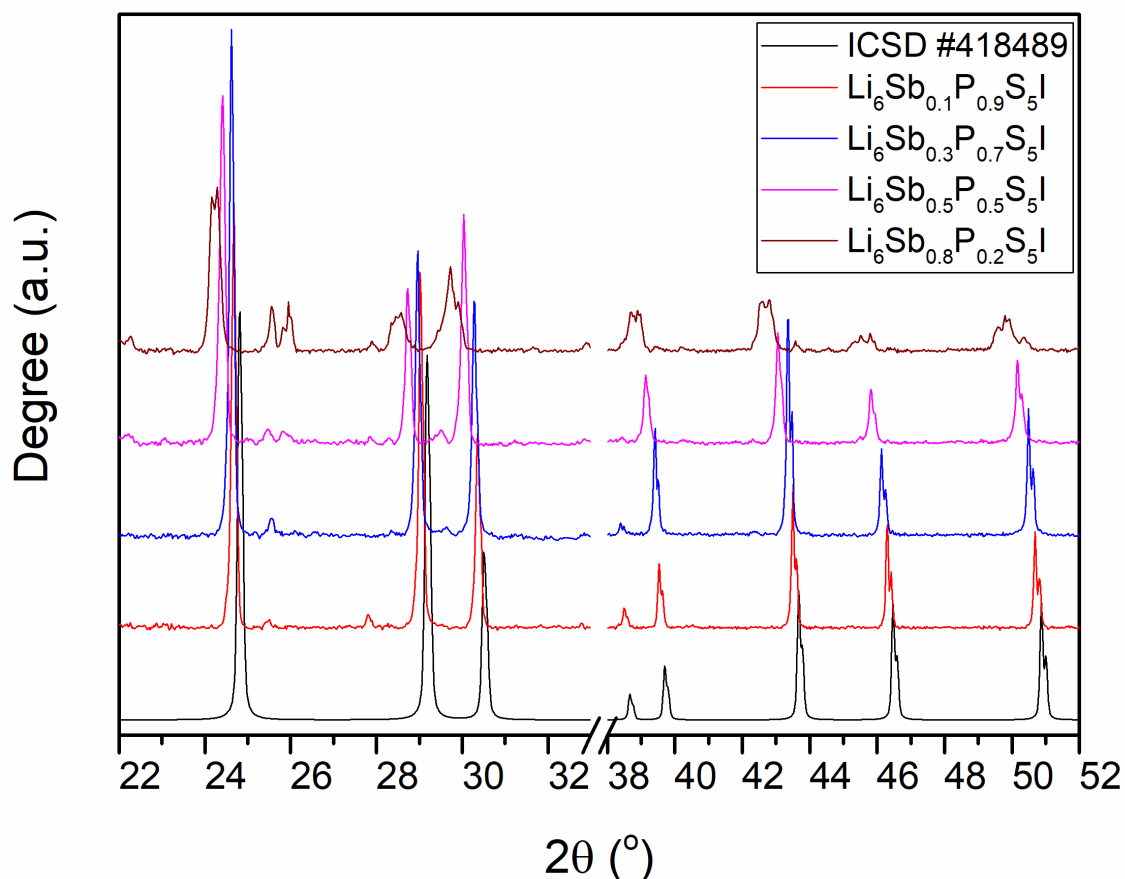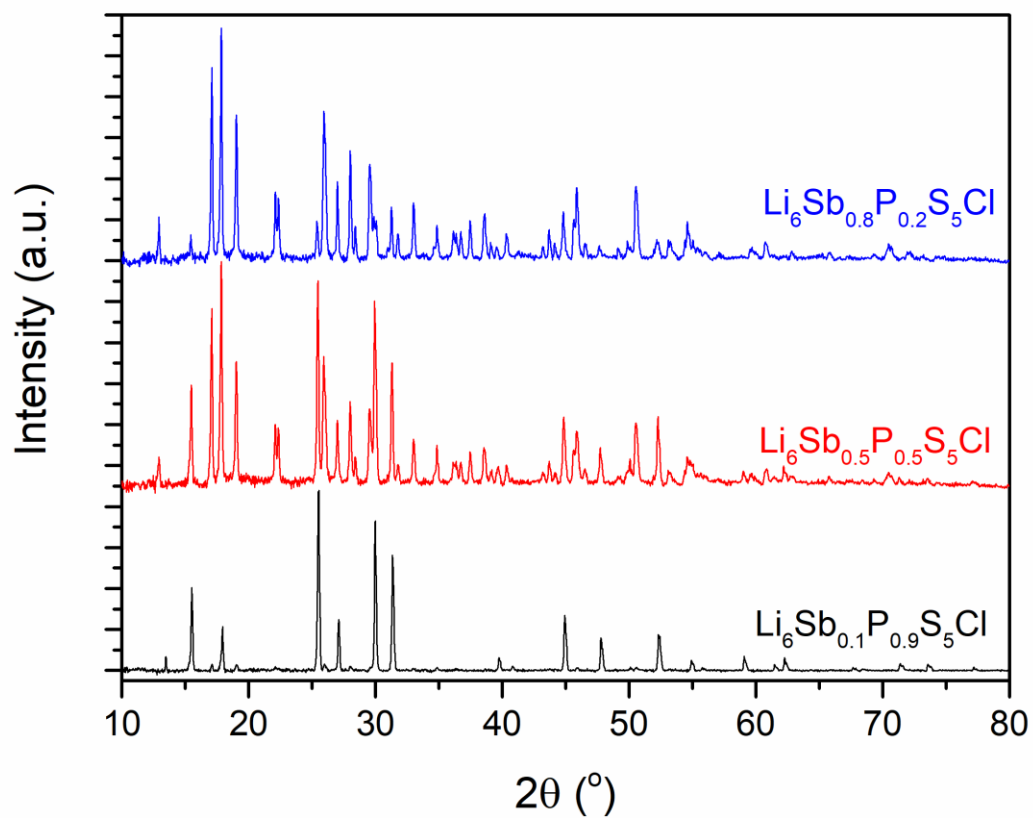**Figure 3.11**: XRD patterns of $Li_6Sb_yP_{1-y}S_5Cl$ (y=0.1, 0.5, 0.8), heat treated at 550^oC for 100h with an ramping rate 5^oC/min.
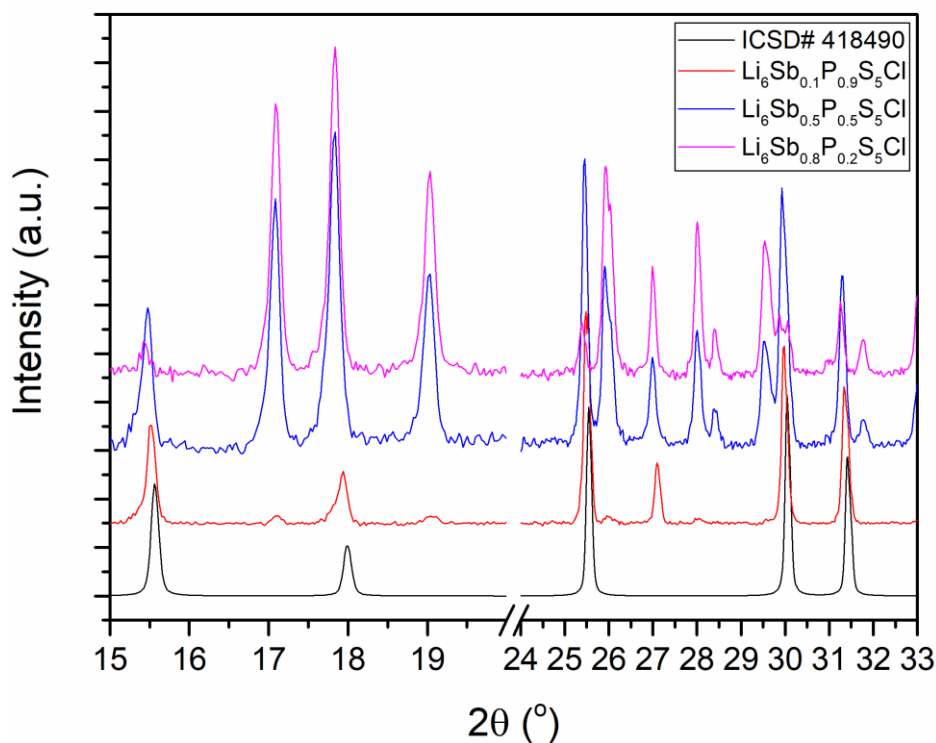
Figure 3.12: Comparison of the XRD patterns of as-synthesized $Li_6Sb_yP_{1-y}S_5Cl$ with argyrodite Li_6PS_5Cl (ICSD #418490).

3.4.3 Summary

Antimony can be successfully doped into the argyrodite Li_6PS_5I with the ionic conductivities increase by one order of magnitude. Higher content doping leads to the formation of impurity phases and lower crystallinity. Lower temperature heat treatment with longer time is possible to give purer phases and higher crystallinity to further increase the Li-ion conductivities. Antimony doped argyrodite Li_6PS_5Cl shows impurities formation at low level doping which indicates the antimony doped argyrodite structure for chlorine phase Li_6PS_5Cl is not stable. Besides, high content doping will lead to longer Li-ion diffusion

61

pathway which may results in low conductivities. Possible low level antimony <10% of argyrodite Li_6PS_5Cl will enlarge the Li-ion pathway which give rise to the ionic conductivities. Meanwhile, this approach can be applied to other thiophosphate solid electrolytes.

3.5 Discussion and Conclusions

In this chapter, I demonstrated a promising direct solution synthesis approach to argyrodite phases Li_6PS_5X (X = Cl, Br) with high ionic conductivities by using THF/ethanol mixtures as the solvents, which is low cost and easy to scale-up. This solution assisted synthesis method of argyrodite Li_6PS_5X (X=Cl, Br, I) can be used to form favorable electrode-electrolyte interface with a large contact area to decrease the interfacial resistance to improve the ASSLBs performance by simply solution coating method.

Antimony doped argyrodite $Li_6Sb_yP_{1-y}S_5I$ results in larger unit cell size with the ionic conductivities increased by one order of magnitude. However, the ionic conductivities are still low for the application in ASSLBs. The possible reason is the I^- is still sitting an the 4a sites which leads to no halogen disorder. Antimony doped argyrodite $Li_6Sb_yP_{1-y}S_5Cl$ leads to the formation of impurity phases at low level antimony doping 10%. However, possible lower level antimony doping <10% will enlarge the Li-ion diffusion pathway which give rise to the ionic conductivities. Besides, antimony doping is a possible method to improve the stability against air and moisture, which is a critical problem for sulfide based solid electrolytes.

Chapter 4 Synthesis of potentially new solid electrolytes $Li_3Y(PS_4)_2$ and $Li_6Y_3(PS_4)_5$

4.1 Introduction

Thiophosphate solid electrolytes have emerged as one of the leading contenders for ASSLBs applications. However, the number of known lithium solid electrolytes remains relatively few and all existing sulfide solid electrolytes suffer from various limitations. For example, LGPS is expensive due to the use of Ge. Thus, it is urgent to develop novel lithium solid electrolytes that have better stability against lithium metal and different cathode materials and are low-cost.

Many of the known lithium thiophosphates with high ionic conductivities have analogues in Ag thiophosphates. For instance, $Li_7P_3S_{11}$ shows remarkable structural similarity with $Ag_7P_3S_{11}$.[89] Inspired by this observation, Ping Ong's group performed a comprehensive screening of the ternary Li-P-S and quaternary Li-M-P-S (M is non-redox-active element) chemical spaces for new lithium solid electrolytes based on high-throughout density functional theory (DFT) calculations. [90] This screening yielded two highly promising candidates $Li_3Y(PS_4)_2$ (E $_{hull}$= 2meV/atom) and $Li_5PS_4Cl_2$ (E $_{hull}$= 17 meV/atom), which are predicted to show excellent phase and electrochemical stability, high Li-ion conductivities, and low electronic conductivity.[90] I am specifically interested in $Li_3Y(PS_4)_2$ due to its high conductivity, possibly better stability and further optimization possibility via aliovalent doping or substitution.

Figure 4.1 shows the crystal structure of $Li_3Y(PS_4)_2$ and the relaxed lattice parameters are given in **Table 4.1**.[90] $Li_3Y(PS_4)_2$ belongs to $C2/c$ space group and have two symmetrically distinct Li sites, which are labeled in **Figure 4.3a**.[90] The ionic conductivity is predicted to be 2.16 mS/cm at RT. The Li ion probability density function (PDF) simulation (**Figure 4.2**) shows the 3D diffusion pathways. Further climbing image nudged elastic band (CI-NEB) calculations show the migration barriers of identified diffusion pathways as showed in **Figure 4.3**. There are five symmetrically distinct hops between neighboring Li sites (**Figure 4.3b, c, d**) and the estimated effective 3D vacancy migration barrier is 268meV.[90] Besides, they showed aliovalent doping can further increase the ionic conductivities. Ca^{2+} and Zr^{4+} with comparable ionic radii to Y^{3+} can be used as dopants to introduce Li-ion interstitials and vacancies respectively. Replacement 12.5% Y^{3+} with Ca^{2+} and Zr^{4+} leads to increase the ionic conductivities to 7.14 and 5.25 mS/cm, and decrease the activation energies to 231 and 241 meV, respectively.[90]

Table 4.1: Relaxed conventional unit cell lattice parameters for $Li_3Y(PS_4)_2$. Reproduced from Ref. 90.

Compound	Atoms/cell	a (Å)	b (Å)	c (Å)	α (º)	β (º)	γ (º)
$Li_3Y(PS_4)_2$	56	17.122	9.290	9.137	90.0	122.3	90.0
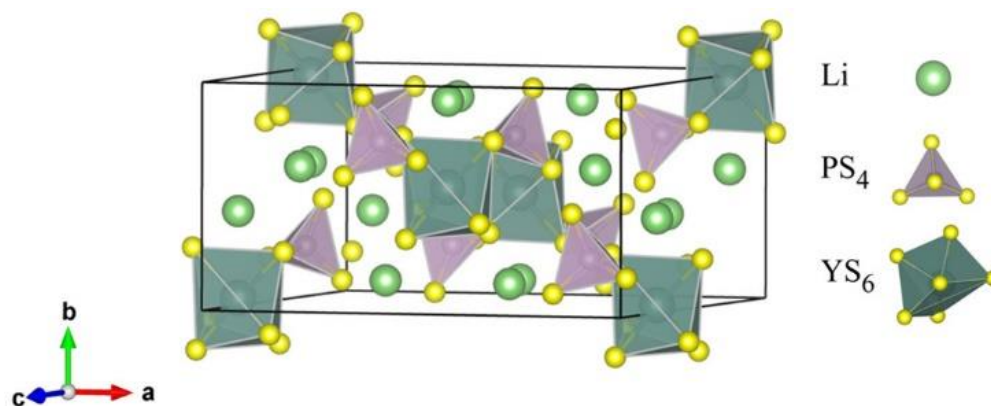
Figure 4.1: Crystal structure (conventional cell) of the identified Li solid electrolyte candidate. Purple tetrahedra, PS_4; dark green octahedral, YS_6; green sphere, Li; yellow sphere, S. reproduced from Ref. 90.

$1 \times 1 \times 2$ supercell of $Li_3Y(PS_4)_2$
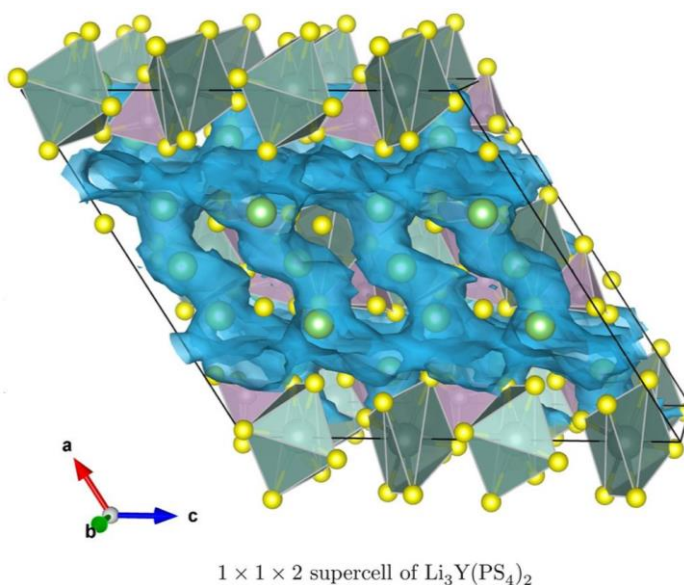
Figure 4.2: Isosurfaces of Li ion probability density distribution P (light blue) for $Li_3Y(PS_4)_2$ from AIMD simulations at 800 K with P= 0.0001 a_0^{-3} (a_0 is the Bohr radius). Reproduced from Ref. 90.
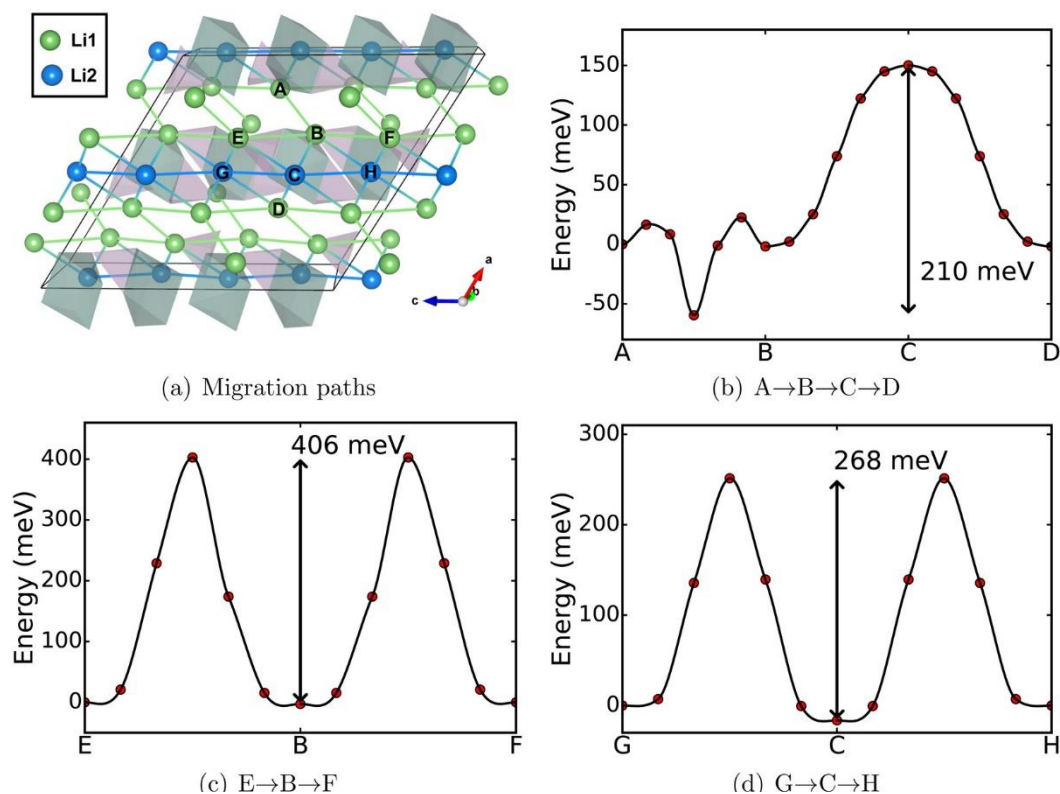
Figure 4.3: (a) Investigated Li vacancy diffusion paths in $Li_3Y(PS_4)_2$ viewed along *b* direction. Symmetrically distinct Li1 and Li2 are represented by green and blue spheres, respectively. Celadon polyhedra and gray tetrahedra indicate YS_6 and PS_4. (b–d) Calculated CI-NEB migration barriers for selected percolating paths. Reproduced from Ref.90.

When searching the reported Li/Ag-Y-P-S structures, I found one other composition $Li_6Y_3(PS_4)_5$[91] ($C12/c1$) which has a similar crystal structure with $Li_3Y(PS_4)_2$ with bigger unit cell, listed in **Table 4.2**. Interestingly, the U_{iso} of the 9 Li sites is extremely high, which indicates the high possibility of high ionic conductivity as showed in **Table 4.3**. Li-ions hoping around in the crystal structure is dramatically important for highly ionic conductivity. Thus, $Li_6Y_3(PS_4)_5$ is potentially a high ionic conductive solid electrolyte. Besides, the same strategy (aliovalent doping as $Li_3Y(PS_4)_2$) can be applied to this phase to further improve the ionic conductivity.

Table 4.2: Unit cell lattice parameters for $Li_6Y_3(PS_4)_5$. Reproduced from Ref. 91.

Compound	a (Å)	b (Å)	c (Å)	α (º)	β (º)	γ (º)
$Li_6Y_3(PS_4)_5$	28.390	10.068	33.715	90.0	113.85	90.0

Table 4.3: Li atomic coordinates in $Li_6Y_3(PS_4)_5$. Reproduced from Ref. 91.

Site	Wyckoff symbol	Symmetry	x	y	z	Occupation	U_{iso}
Li1	8*f*	1	0.4575	0.393	0.8061	1	0.0550
Li2	8*f*	1	0.6713	0.383	0.6722	1	0.0610
Li3	8*f*	1	0.5403	0.714	0.6747	1	0.0970
Li4	8*f*	1	0.1789	0.238	0.7096	1	0.0830
Li5	8*f*	1	0.4125	0.738	0.5544	1	0.1110
Li6	8*f*	1	0.2659	0.815	0.5435	1	0.1240
Li7	8*f*	1	0.2394	0.134	0.5516	1	0.1390
Li8	8*f*	1	0.2058	0.443	0.5997	1	0.1350
Li9	8*f*	1	0.492	0.978	0.695	1	0.1800

4.2 Synthesis and Characterization

ZrS_2 were synthesized by reacting elemental Zr and sulfur. Zr powder and sulfur (Sigma Aldrich ≥99.5%) are mixed in stoichiometric proportions of ZrS_2 and the powders were pressed into 13mm pellets, transferred into a quartz tube and then sealed under vacuum. Finally, the sample was heat treated at 900ºC for 24h with an increasing rate 0.5ºC/min and a decreasing rate 5ºC/min.

Li_2S (Sigma Aldrich 99.98%), P_2S_5 (Sigma Aldrich 99%), Y_2S_3 (Alfa Aesar 99.9%), CaS (Alfa Aesar 99%), as-synthesized ZrS_2 were used as starting materials and mixed in

stoichiometric proportions to yield global compositions of $Li_3Y(PS_4)_2$, $Li_6Y_3(PS_4)_5$, $Li_{6+x}Ca_xY_{3-x}(PS_4)_5$, and $Li_{6-x}Zr_xY_{3-x}(PS_4)_5$ inside an argon filled glovebox. The powder after ground were then cold pressed at 2 tons into 13mm diameter pellets. The pellets were then transferred into carbon coated quartz tubes and sealed under vacuum. Finally, the samples were crystallized at different temperatures, time, and ramping rate.

X-ray diffraction (XRD) measurements were conducted at room temperature on a PANalytical Empyrean diffractometer with Cu-Kα radiation equipped with a PIXcel bidimensional detector. XRD patterns for phase identification were obtained in the Bragg-Brentano geometry, with samples placed on a zero-background sample holder in an Ar-filled glovebox and protected by Kapton film.

The ionic conductivities were measured by the electrochemical impedance spectroscopy (EIS) with a home-built setup. Typically, 100 mg of the glass ceramic sample powders were placed between two stainless steel rods and pressed into a 10 mm diameter pellet by a hydraulic press at 2T for 3 min in an Ar-filled glovebox. EIS was performed with 20 mV constant voltage within a frequency range of 1 MHz-10 mHz using the VMP3 potentiostat/galvanostat (Bio-logic).

4.3 Results and Discussion

Figure 4.4 shows the XRD patterns of $Li_3Y(PS_4)_2$ with different heat treatment temperatures. Compared to the simulated pattern of $Li_3Y(PS_4)_2$, there is no any pattern matched the desired one. However, the pattern heat treated at 700°C is similar to the $Li_6Y_3(PS_4)_5$ which leads to synthesis of $Li_6Y_3(PS_4)_5$. **Figure 4.5** shows the XRD pattern of $Li_6Y_3(PS_4)_5$ heat

treated at 700°C for 10h with an increasing rate 5°C/min and a decreasing rate 1°C/min which matches the simulated pattern from the cif file (ICSD# 417653) exactly. The EIS result for $Li_6Y_3(PS_4)_5$ was shown in **Figure 4.6a** which corresponding to the ionic conductivity of 3.6×10^{-6} S/cm. Due to the low ionic conductivity, aliovalent doping Ca^{2+} and Zr^{4+} were tried to improve the conductivity as indicated in Ping Ong's work.
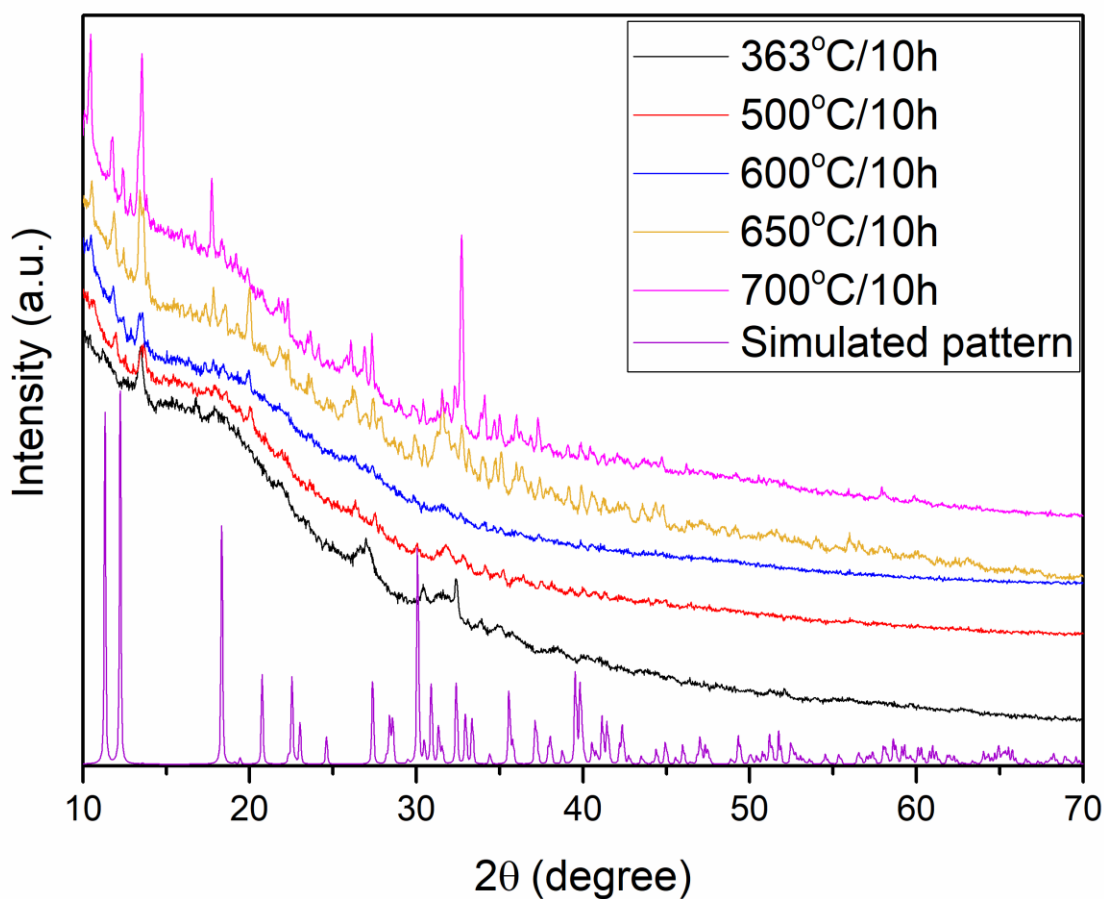

Figure 4.4: Comparison of XRD patterns of $Li_3Y(PS_4)_2$ with different heat treatment temperatures as labeled to the simulated pattern (Ramping rate 5°C/min).

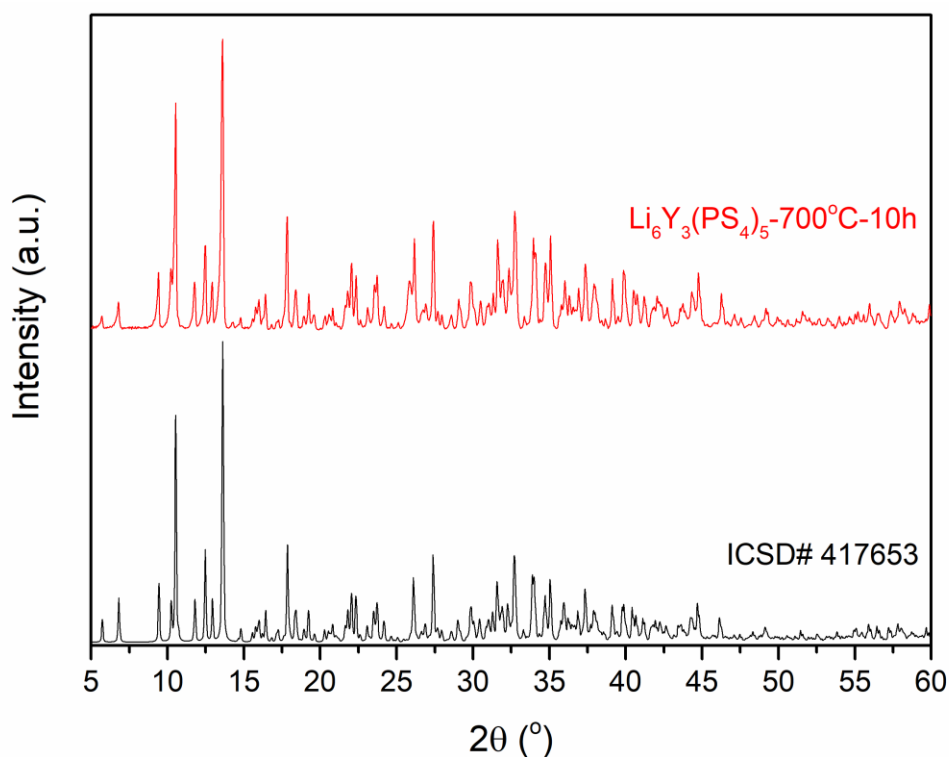**Figure 4.5**: Comparison of $Li_6Y_3(PS_4)_5$ heat treated at 700°C for 10h with a decreasing rate 1°C/min with the pattern simulated from cif file (ICSD# 417653).

Table 4.4: Calculated ionic conductivities of the non-doped, Ca-doped, and Zr-doped $Li_6Y_3(PS_4)_5$.

Sample	Conductivity
Un-heat treated mixed precursors	4.3×10^{-6} S/cm
$Li_6Y_3(PS_4)_5$-5°C/min(Increase)-700-10h-1°C/min(Decrease)	3.6×10^{-6} S/cm
$Li_{6.3}Ca_{0.3}Y_{2.7}(PS_4)_5$-5°C/min(Increase)-700-10h-1°C/min(Decrease)	5.0×10^{-6} S/cm
$Li_{6.6}Ca_{0.6}Y_{2.4}(PS_4)_5$-5°C/min(Increase)-700-10h-1°C/min(Decrease)	6.9×10^{-6} S/cm
$Li_{6.9}Ca_{0.9}Y_{2.1}(PS_4)_5$-5°C/min(Increase)-700-10h-1°C/min(Decrease)	4.5×10^{-6} S/cm
$Li_{7.2}Ca_{1.2}Y_{1.8}(PS_4)_5$-5°C/min(Increase)-700-10h-1°C/min(Decrease)	6.7×10^{-6} S/cm
$Li_{5.85}Zr_{0.15}Y_{2.85}(PS_4)_5$-5°C/min(Increase)-700-10h-5°C/h(Decrease)	1.93×10^{-6} S/cm
$Li_{5.7}Zr_{0.3}Y_{2.7}(PS_4)_5$-5°C/min(Increase)-700-10h-5°C/h(Decrease)	2.26×10^{-6} S/cm
$Li_{5.4}Zr_{0.6}Y_{2.4}(PS_4)_5$-5°C/min(Increase)-700-10h-5°C/h(Decrease)	2.09×10^{-6} S/cm
$Li_{5.1}Zr_{0.9}Y_{2.1}(PS_4)_5$-5°C/min(Increase)-700-10h-5°C/h(Decrease)	4.21×10^{-6} S/cm
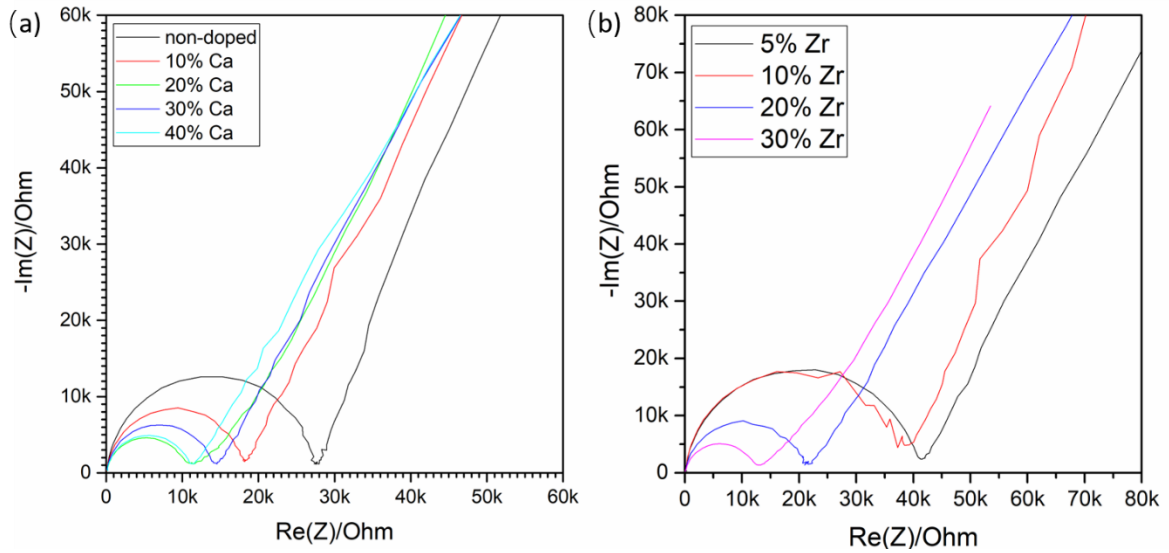
Figure 4.6: EIS measurements of (a) non-doped, 10% ($Li_{6.3}Ca_{0.3}Y_{2.7}(PS_4)_5$), 20% ($Li_{6.6}Ca_{0.6}Y_{2.4}(PS_4)_5$), 30% ($Li_{6.9}Ca_{0.9}Y_{2.1}(PS_4)_5$), 40% Ca ($Li_{7.2}Ca_{1.2}Y_{1.8}(PS_4)_5$) doped $Li_6Y_3(PS_4)_5$ (Heat treated at 700oC for 10h with an increasing rate 5°C/min and a decreasing rate 1°C/min); (b) 5% ($Li_{5.85}Zr_{0.15}Y_{2.85}(PS_4)_5$), 10% ($Li_{5.7}Zr_{0.3}Y_{2.7}(PS_4)_5$), 20% ($Li_{5.4}Zr_{0.6}Y_{2.4}(PS_4)_5$), 30% ($Li_{5.1}Zr_{0.9}Y_{2.1}(PS_4)_5$)doped $Li_6Y_3(PS_4)_5$ (Heat treated at 700°C for 10h with an increasing rate 5°C/min and a decreasing rate 5°C/h).

The XRD patterns of Ca-doped $Li_6Y_3(PS_4)_5$ were shown in **Figure 4.7**. With different contents of Ca doping, the XRD patterns still match the simulated pattern with intensity change on some peaks. The monoclinic structure leads to plenty of peaks, which is difficult to determine whether there are impurities formation. However, there are two peaks forms at 8.7° and 14.0° and the intensity of these two peaks start to increase with the increasing content of Ca, except the 30% Ca. The EIS measurements were shown in **Figure 4.6a** and the conductivities of these Ca-doped $Li_6Y_3(PS_4)_5$ did not increase the conductivities much. Even though there are possibly impurities formation, the right shifted (high theta) peaks indicate Ca is doped into the structure. However, Ca^{2+} has bigger size the Y^{3+}, replacement Y^{3+} with Ca^{2+}

71

should lead bigger unit cell which corresponding to left shifted (low theta) peaks. Thus, Ca^{2+} may not go into the Y^{3+} sites.
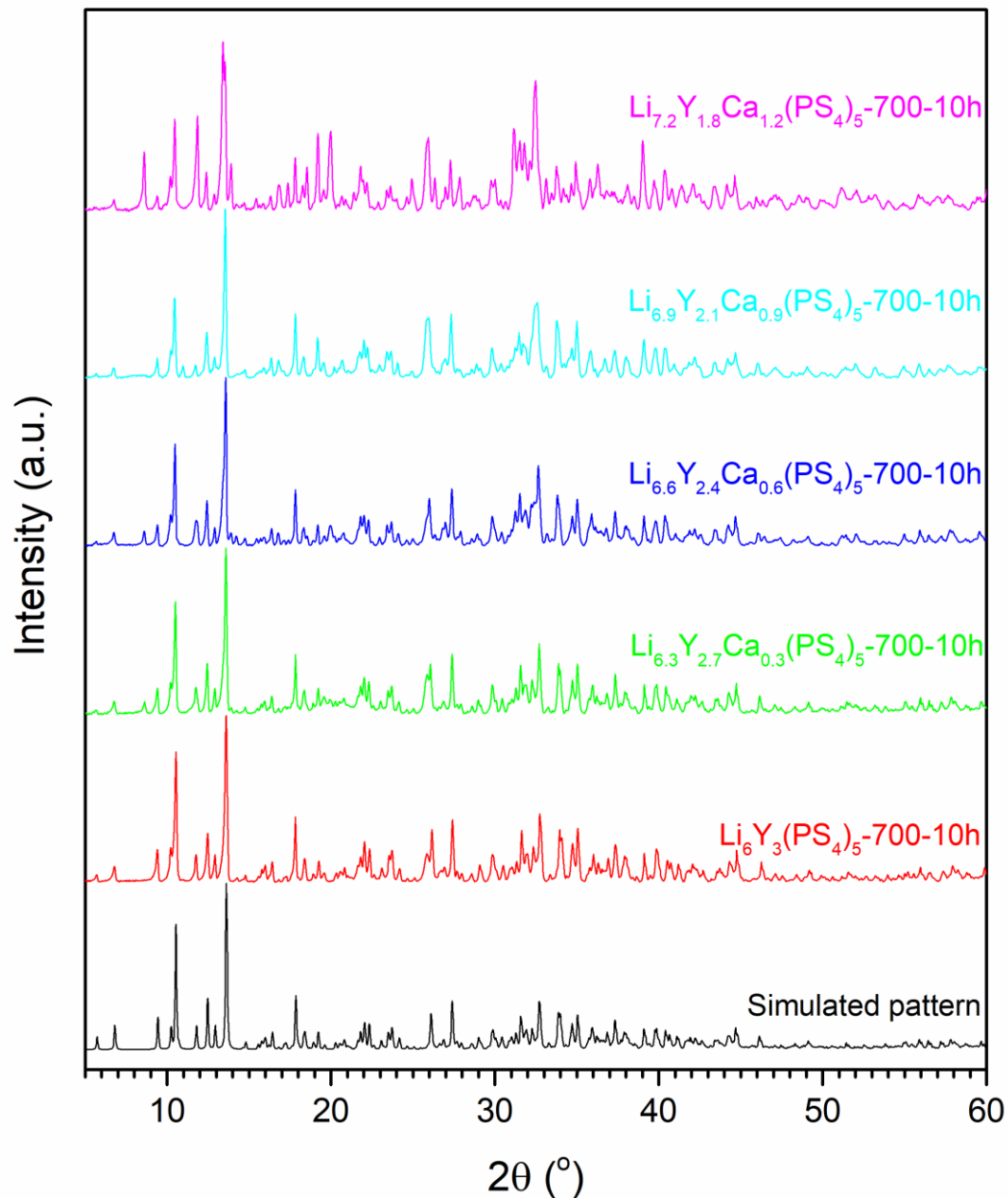
Figure 4.7: Comparison of XRD patterns of 10% $Li_{6.3}Ca_{0.3}Y_{2.7}(PS_4)_5$, 20% $Li_{6.6}Ca_{0.6}Y_{2.4}(PS_4)_5$, 30% $Li_{6.9}Ca_{0.9}Y_{2.1}(PS_4)_5$, 40% $Li_{7.2}Ca_{1.2}Y_{1.8}(PS_4)_5$ (Heat treated at 700°C for 10h with an 5°C/min increasing rate and a 1°C/min decreasing rate) with simulated pattern.

As Ca-doping did not increase the conductivities much, Zr-doping which can increase the Li-ion vacancy concentration should potentially increase the conductivity greatly. **Figure 4.8** shows the XRD patterns of Zr-doped $Li_6Y_3(PS_4)_5$, heat treated at 700^oC for 10h with a $5^oC/min$ increasing rate and a $5^oC/h$ decreasing rate. The patterns also match the simulated pattern. The intensity of some peaks changes with different content of Zr-doping. A new peak at 9.9^o starts to form with low content of Zr-doping and the intensity increases with the increasing content of Zr. Meanwhile, the peaks also shift to the right (high theta) continuously with the increasing content of Zr, which indicates Zr was successfully doped into the structure. The EIS measurements were shown in **Figure 4.6b** and the ionic conductivities were summarized in **Table 4.4**. The conductivities slightly decreased.

4.4 Summary

In this chapter, I investigated the synthesis of $Li_3Y(PS_4)_5$ and $Li_6Y_3(PS_4)_5$. $Li_3Y(PS_4)_2$ have not been successfully synthesized. However, $Li_6Y_3(PS_4)_5$ was successfully synthesized with low ionic conductivity ~10^{-6} S/cm. Aliovalent doping (Ca^{2+} and Zr^{4+}) which can increase Li-ion interstitials and vacancies were tried to further improve the ionic conductivities. However, the aliovalent doping didn't increase the conductivity much, which may be caused by the relatively low crystallinity. As the samples melt at 700^oC to help the Zr and Ca doping, low temperature decreasing rate did not help crystalize the samples well. Further lower temperature, longer time heat treatment can possible increase the crystallinity to further increase the ionic conductivities. As $Ag_3Y(PS_4)_2$ was reported,[91] it will be synthesized by following the reported procedures. Ionic exchange of Ag^+ with Li^+ will be performed to

determine whether $Li_3Y(PS_4)_2$ phase is stable and exists and also investigate the ionic conductivities of this phase.
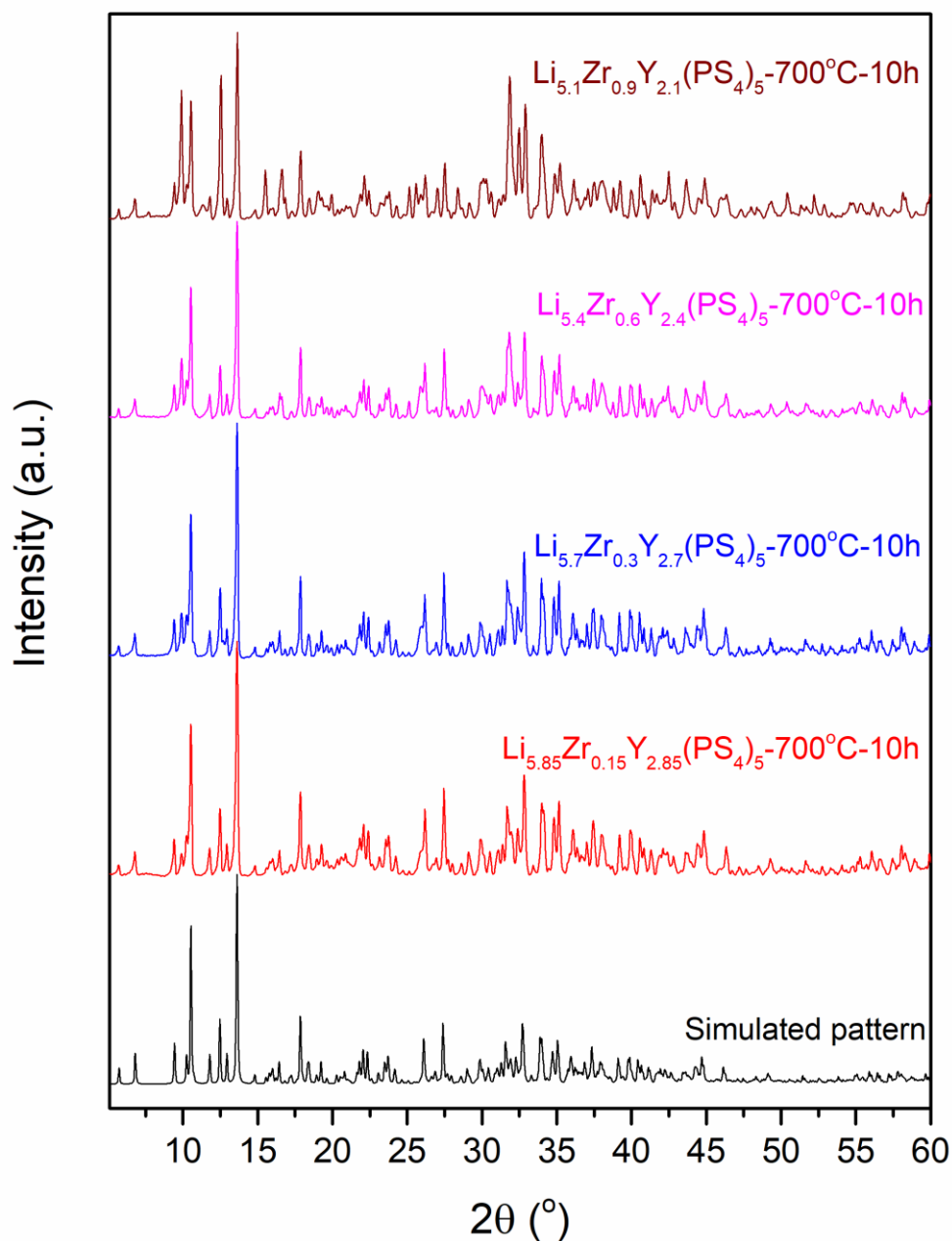
Figure 4.8: Comparison of XRD patterns of 5% $Li_{5.85}Zr_{0.15}Y_{2.85}(PS_4)_5$, 10% $Li_{5.7}Zr_{0.3}Y_{2.7}(PS_4)_5$, 20% $Li_{5.4}Ca_{0.6}Y_{2.4}(PS_4)_5$, 30% $Li_{5.1}Zr_{0.9}Y_{2.1}(PS_4)_5$ (Heat treated at 700°C for 10h with an 5°C/min increasing rate and a 5°C/h decreasing rate) with simulated pattern.

Future Perspectives

The work presented in this thesis will potentially bring the ASSLBs one step closer towards commercialization. The key factors to realize ASSLBs are a superior solid electrolyte with high ionic conductivity, good chemical and electrochemical stability, low interfacial resistance, as well as to be synthesized in large scales at low costs.

Chapter 3 shows a promising direct solution synthesis approach for the argyrodite phases Li_6PS_5X (X=Cl, Br, I) with THF/ethanol mixtures as the solvents. The resulting Li_6PS_5Cl and Li_6PS_5Br show high conductivities up to 10^{-3} S/cm. The ~15 wt% Li_3PO_4, although presents as the impurity under current conditions, may be obtained as a coating on the Li_6PS_5X particles with modified synthesis methods. This would improve the electrolyte stability against high voltage cathodes and the lithium metal anode. The initial low conductivity of Li_6PS_5I (~10^{-7} S/cm) was improved by antimony doping on the P site, demonstrating the key role of unit cell size and halogen disorder on the Li^+ conductivity in the argyrodite lattice. Nevertheless, inspired by the high conductivity of the Na_3SbS_4 phase, this x $LiCl - (1-x) Li_3SbS_4$ (x=0~1) family, could be another choice of solid electrolytes. The effort of synthesizing the pure phase is worth to carry out in further studies.

Chapter 4 focuses on the synthesis of two new solid electrolytes $Li_3Y(PS_4)_2$ and $Li_6Y_3(PS_4)_5$. $Li_3Y(PS_4)_2$ is predicted to be highly conductive by simulation, while $Li_6Y_3(PS_4)_5$ shows extremely high U_{iso} for Li^+ which makes it a potential Li superionic conductors. The $Li_6Y_3(PS_4)_5$ obtained from solid state synthesis showed a low conductivity of 3.6×10^{-6} S/cm which did not improve with aliovalent Ca^{2+}, Zr^{4+} doping on Y^{3+}. The low crystallinity of the

products could be the key reason for low ionic conductivity. Further modification on the synthesis conditions, such as lower temperature and longer heat time, could potentially help improve the crystallinity and increase the conductivities. The $Li_3Y(PS_4)_2$, on the other hand, has not been successfully synthesized. All attempts resulted in the more stable $Li_6Y_3(PS_4)_5$ phase. Ion exchange of Ag^+ with Li^+ for the stable $Ag_3Y(PS_4)_2$ phase could be a promising way to synthesize $Li_3Y(PS_4)_2$. For both $Li_6Y_3(PS_4)_5$ and $Li_3Y(PS_4)_2$, if satisfactory ionic conductivities are obtained for the pure phases, future work can be focused on the development of easier synthesis method and investigation of interfacial stability against different cathodes and the lithium metal anode.

There is a long way to go before the practical implementation of ASSLBs at the present industrial level. With the already proposed solid electrolyte candidates, steps need to be taken to reduce the production cost, improve the mechanical properties, and overcome the charge transfer resistance barrier at the solid-solid interface between the electrodes and solid electrolytes. Meanwhile, the discovery of new solid electrolytes with high conductivity, good electrochemical stability and acceptable mechanical properties is also necessary to provide alternative choices for ASSLBs.

Reference

1, J. B. Goodenough, Y. Kim, *Chem. Mater.* **2010**, 22, 587.

2, J. B. Goodenough, K. S. Park, *J. Am. Chem. Soc.* **2013**, 135, 1167.

3, K. Brandt, *Solid State Ionics*, **1994**, 69, 173.

4, B. L. Ellis, K. T. Lee, L. F. Nazar, *Chem. Mater.*, **2010**, 22, 691.

5, Tarascon, J. M.; Armand, M. *Nature* **2001**, 414, 359

6, L. F. Nazar, M. Cuisinier, Q. Pang, *MRS Bull.*, **2014**, 39, 436.

7, J. G. Kim, B. Son, S. Mukherjee, N. Schuppert, A. Bates, O. Kwon, M. J. Choi, M. H. Y. Chung, S. Park, *J. Power Sources* **2015**, *282*, 299-322.

8, X. Liang, Q. Pang, I. R. Kochetkov, M. S. Sempere, H. Huang, X. Sun, L. F. Nazar, *Nature Energy* **2017**, 2, 17119.

9, N. S. Choi, Z. Chen, S. A. Freunberger, X. Ji, Y. K. Sun, K. Amine, G. Yushin, L. F. Nazar, J. Cho, P. G. Bruce, *Angew. Chem. Int. Ed.*, **2012**, 51, 9994.

10, M.S. Whittingham, *Chem. Rev.*, **2004**, 104, 4271.

11, S. Evers, L. F. Nazar, Acc. *Chem. Res.*, **2012**, 46, 1135.

12, A. Manthiram, Y. Fu, Y.-S. Su, *Acc. Chem. Res.*, **2012**, 46, 1125.

13, A. Rosenman, E. Markevich, G. Salitra, D. Aurbach, A. Garsuch, F. F. Chesneau, *Adv. Energy Mater.*, **2015**, 5, 1500212.

14, Q. Pang, X. Liang, C.Y. Kwok, L.F. Nazar, *Nat. Energy*, **2016**, 1, 16132.

15, H. Guang, S. Evers, X. Liang, M. Cuisinier, A. Garsuch, L. F. Nazar, *ACS Nano,* **2013**, 7, 10920.

16, X. Ji, K. T. Lee, L. F. Nazar, *Nat. Mater.*, **2009**, 8, 500.

17, G. He, S. Evers, X. Liang, M. Cuisinier, A. Garsuch, L. F. Nazar, *ACS Nano*, **2013**, **7**, 10920.

18, N. Jayaprakash, J. Shen, S. S. Moganty, A. Corona, L.A. Archer, *Angew. Chem. Int. Ed.*, **2011**, 50, 5904.

19, F. Bottger-Hiller, P. Kempe, G. Cox, A. Panchenko, N. Janssen, A. Petzold, T. Thurn-Albrecht, L. Borchardt, M. Rose, S. Kaskel, C. Georgi, H. Lang, S. Spange, *Angew. Chem. Int. Ed.*, **2013**, 52, 6088.

20, J. Schuster, G. He, B. Mandlmeier, T. Yim, K. T. Lee, T. Bein, L. F. Nazar, *Angew. Chem. Int. Ed.*, **2012**, 51, 3591.

21, L. Sun, M. Li, Y. Jiang, W. Kong, K. Jiang, J. Wang, S. Fan, *Nano Lett.*, **2014**, 14, 4044.

22, J. Song, M. L. Gordin, T. Xu, S. Chen, Z. Yu, H. Sohn, J. Lu, Y. Ren, Y. Duan, D. Wang, *Angew. Chem. Int. Ed.*, **2015**, 54, 4325.

23, X. Ji, S. Evers, R. Black, L. F. Nazar, *Nat. Commun.*, **2011**, 2, 325.

24, K. T. Lee, R. Black, T. Yim, X. Ji, L. F. Nazar, *Adv. Energy Mater.*, **2012**, 2, 1490.

25, Z. Xiao, Z. Yang, L. Wang, H. Nie, M. Zhong, Q. Lai, X. Xu, L. Zhang, S. Huang, *Adv. Mater.*, **2015**, 27, 2891.

26, Q. Pang, D. Kundu, M. Cuisinier, L. F. Nazar, *Nat. Commun.*, **2014**, 5, 4759.

27, X. Liang, C. J. Hart, Q. Pang, A. Garsuch, T. Weiss, L. F. Nazar, *Nat. Commun*., **2015**, 6, 5682.

28, E. Quartarone and P. Mustarelli, *Chem. Soc. Rev.* 2011, **40**, 2525-2540.

29, Y. Hu, *Nat. Energy* 2016, **1**, 16042-16043.

30, J. W. Fergus, *J. Power Sources, 2010,* **195**, 4554-4569.

31, T. Matsuyama, A. Sakuda, A. Hayashi, Y. Togawa, S. Mori and M. Tatsumisago, *J. Solid State Electrochem.*, 2013, **17**, 2697-2701.

32, J. Bates, N. Dudney, B. Neudecker, A. Ueda, C. Evans, *State Ionics*, **2000**, 135, 33.

33, V. Thangadurai, W. Weppner, *Ionics*, **2006**, 12, 81.

34, A. Manthiram, X. Yu, S. Wang, S., *Nat. Rev. Mater.*, **2017**, 2, 16103.

35, R. Murugan, V. Thangadurai, W. Weppner, *Angew. Chem. Int. Ed.*, **2007**, 46, 7778.

36, M. Itoh, Y. Inaguma, W. H. Jung, L. Chen, T. Nakamura, *Solid State Ionics*, **1994**, 70, 203.

37, H. Aono, E. Sugimoto, Y. Sadaoka, N. Imanaka, G. Y. Adachi, *J. Electrochem. Soc.,* **1990**, 137, 1023.

38, J. Fu, *Solid State Ionics*, **1997**, 96, 195.

39, J. Fu, *Solid State Ionics*, **1997**, 104, 191.

40, M. Murayama, R. Kanno, M. Irie, S. Ito, T. Hata, N. Sonoyama, Y. Kawamoto, *J. Solid State Chem.*, **2002**, 168, 140.

41, R. Kanno, M. Murayama, M., *J. Electrochem. Soc.*, *2001*, 1148, A742.

42, F. Mizuno, A. Hayashi, K. Tadanaga, M. Tatsumisago, *Solid State Ionics*, **2006**, 177, 2721.

43, Y. Seino, T. Ota, K. Takada, A. Hayashi, M. Tatsumisago, *Energy Environ. Sci.,* **2014**, 7, 627.

44, N. Kamaya, K. Homma, Y. Yamakawa, M. Hirayama, R. Kanno, M. Yonemura, T. Kamiyama, Y. Kato, S. Hama, K. Kawamoto, K., *Nat. Mater.,* **2011**, 10, 682.

45, P. Bron, S. Johansson, K. Zick, J. Schmedt auf der Günne, S. Dehnen, B. Roling, J. *Am. Chem. Soc.*, **2013**, 135, 15694.

46, S. Boulineau, M. Courty, J. M. Tarascon, V. Viallet, *Solid State Ionics*, **2012**, 221, 1.

47, Y. Kato, S. Hori, T. Saito, K. Suzuki, M. Hirayama, A. Mitsui, M. Yonemura, H. Iba, R. Kanno, *Nat. Energy*, **2016**, 1, 16030.

48, S. J. Sedlmaier, S. Indris, C. Dietrich, M. Yavuz, C. Dräger, F. von Seggern, H. Sommer, J. Janek, *Chem. Mater.*, **2017**, 29,1830.

49, Z. Liu, W. Fu, E. A. Payzant, X. Yu, Z. Wu, N. J. Dudney, J. Kiggans, K. Hong, A. J. Rondinone, C. Liang, *J. Am. Chem. Soc.*, **2013**, 135, 975.

50, E. Rangasamy, Z. Liu, M. Gobet, K. Pilar, G. Sahu, W. Zhou, H. Wu, S. Greenbaum, C. Liang, *J. Am. Chem. Soc.*, **2015**, 137, 1384.

51, H. P. Hong, *Mater. Res. Bull.*, **1978**, 13, 117.

52, K. Takada, *Acta Mater.*, **2013**, 61, 759.

53, A. Yamauchi, A. Sakuda, A. Hayashi, M. Tatsumisago, *J. Power Sources*, **2013**, 244, 707.

54, N. Aotani, K. Iwamoto, K. Takada, S. Kondo, *Solid State Ionics*, **1994**, 68, 35.

55, Z. Zhang, J. H. Kennedy, *Solid State Ionics*, **1990**, 38, 217.

56, R. Sakamoto, M. Tatsumisago, T. Minami, *J. Phys. Chem. B,* **1999**, 103, 4029.

57, R. Mercier, J. P. Malugani, B. Fahys, G. Robert, *Solid State Ionics*, **1981**, 5, 663.

58, J. H. Kennedy, Z. Zhang, *J. Electrochem. Soc.*, **1988**, 135, 859.

59, T. Minami, A. Hayashi, M. Tatsumisago, *Solid State Ionics*, **2006**, 177, 2715.

60, M. Ribes, B. Barrau, J. Souquet, *J. Non-Cryst. Solids*, **1980**, 38, 271.

61, H. Wada, M. Menetrier, A. Levasseur, P. Hagenmuller, *Mater. Res. Bull.*, **1983**, 18, 189.

62, Y. Mo, S. P. Ong, G. Ceder, *Chem. Mater.*, **2011**, 24, 15.

63, Y. Zhao, Y. Ding, Y. Li, L. Peng, H. R. Byon, J. B. Goodenough, G. Yu, *Chem. Soc. Rev.,* **2015**, 44, 7968.

64, S. Ito, M. Nakakita, Y. Aihara, T. Uehara, N. Machida, *J. Power Sources* **2014**, *271*, 342.

65, Y. Zhu, X. He, Y. Mo, *ACS Appl. Mater. Interfaces*, **2015**, 7, 23685.

66, W. D. Richards, L. J. Miara, Y. Wang, J. C. Kim, G. Ceder, *Chem. Mater.*, **2015**, 28, 266.

67, J. Auvergniot, A. Cassel, J. B. Ledeuil, V. Viallet, V. Seznec, R. Dedryvère, *Chem. Mater.*, **2017**, 29, 3883.

68, S. Wenzel, S. J. Sedlmaier, C. Dietrich, W. G. Zeier, J. Janek, *Solid State Ionics*, 2017, DOI:10.1016/j.ssi.2017.07.005.

69, B. H. Toby, R. B. Von Dreele, *J. Applied Crystallography*, **2013**, 46, 544.

70, J. Rodriguez-Carvajal, *Physica B.*, **1993**, 192, 55.

71, P. Knauth, *Solid State Ionics*, 2009, **180**, 911.

72, A. Sakuda, A. Hayashi and M. Tatsumisago, *Sci. Rep.*, 2013, **3**, 2261.

73, J. E. Ni, E. D. Case, E. J. S. Sakamoto, E. Rangasamy and J. B. Wolfenstine, *J. Mater. Sci.*, 2012, **47**, 7978.

74, R. P. Rao, N. Sharma, V. Peterson and S. Adams, *Solid State Ionics*, 2013, **230**, 72.

75, M. Chen, R. P. Rao and S. Adams, *Solid State Ionics*, 2014, **262**, 183.

76, M. Chen, R. P. Rao and S. Adams, *Solid State Ionics*, 2014, **268**, 300.

77, M. Chen, X. Yin, M. V. Reddy and S. Adams, *J. Mater. Chem. A*, 2015, **3**, 10698.

78, M. Chen and S. Adams, *J. Solid State Electrochem.*, 2015, **19**, 697.

79, J. Auvergniot, A. Casse, J. B. Ledeuil, V. Vialllet, V. Seznec and R. Dedryvère, *Chem. Mater.*, 2017, **29**, 3883.

80, C. Yu, S. Ganapathy, N. J. J. de Klerk, I. Roslon, E. R. H. van Eck, A. P. M. Kentgens, M. Wagemaker, *J. Am. Chem. Soc.*, 2016, **138**, 11192.

81, N. J. J. de Klerk, I. Rosłoń, M. Wagemaker, *Chem. Mater.*, **2016**, 28, 7955.

82, H. J. Deiseroth, S. T. Kong, H. Eckert, J. Vannahme, C. Reiner, T. Zaiss, M. Schlosser, *Angew. Chem., Int. Ed.*, **2008**, 47, 755.

83, P. R. Rayavarapu, N. Sharma, V. K. Peterson, S. Adams, *J. Solid State Electrochem.,* **2012**, 16, 1807.

84, M. A. Kraft, S. P. Culver, M. Calderon, F. Böcher, T. Krauskopf, A. Senyshyn, C. Dietrich, A. Zevalkink, J. Janek, W. G. Zeier, *J. Am. Chem. Soc.*, **2017**, 139, 10909.

85, S. Yubuchi, S. Teragawa, K. Aso, K. Tadanaga, A. Hayashi, M. Tatsumisago, *J. Power Sources*, 2015, **293**, 941.

86, O. Pecher, S. Kong, T. Goebel, V. Nickel, K. Weichert, C. Reiner, H. Deiseroth, J. Maier, F. Haarmann and D. Zahn, *Chem. Eur. J.*, 2010, **16**, 8347-8354.

87, H. M. Rietveld, *J. Appl. Cryst.*, 1969, **2**, 65-71.

88, S. T. Kong, H. J. Deiseroth, J. Maier, V. Nickel, K. Weichert, C. Reiner, *Z. Anorg. Allg. Chem.*, **2010**, 636, 1920.

89, H. Yamane, M. Shibata, Y. Shimane, T. Junke, Y. Seino, S. Adams, K. Minami, A. Hayashi, M. Tatsumisago, *Solid State Ionics*, **2007**, 178, 1163.

90, Z. Zhu, I. H. Chu, S. P. Ong, *Chem. Mater.*, **2017**, 29, 2474.

91, C. Müller, S. Jörgens, A. and Mewis, *Z. Anorg. Allg. Chem.*, **2007**, 633,1633.